FLASH: Faint Lenses from Associated Selection with *Herschel*

Tom J. L. C. Bakx [1,2,3]★ Bethany S. Gray,[4] Joaquin González-Nuevo [5,6] Laura Bonavera,[5,6]
Aristeidis Amvrosiadis,[7] Stephen Eales,[8] Masato Hagimoto [2] and Stephen Serjeant [9]

[1] *Department of Space, Earth, & Environment, Chalmers University of Technology, Chalmersplatsen 4, Gothenburg SE-412 96, Sweden*
[2] *Department of Physics, Graduate School of Science, Nagoya University, Aichi 464-8602, Japan*
[3] *National Astronomical Observatory of Japan, 2-21-1, Osawa, Mitaka, Tokyo 181-8588, Japan*
[4] *Department of Architecture & Civil Engineering, University of Bath, Claverton Down, Bath BA2 7AY, UK*
[5] *Departamento de Fisica, Universidad de Oviedo, C. Federico Garcia Lorca 18, Oviedo E-33007, Spain*
[6] *Instituto Universitario de Ciencias y Tecnologas Espaciales de Asturias (ICTEA), C. Independencia 13, Oviedo E-33004, Spain*
[7] *Institute for Computational Cosmology, Durham University, South Road, Durham DH1 3LE, UK*
[8] *School of Physics and Astronomy, Cardiff University, The Parade, Cardiff CF24 3AA, UK*FLASH: Faint Lenses from Associated Selection with Herschel
[9] *School of Physical Sciences, The Open University, Milton Keynes MK7 6AA, UK*

ABSTRACT
We report the ALMA Band 7 observations of 86 *Herschel* sources that likely contain gravitationally lensed galaxies. These sources are selected with relatively faint 500 μm flux densities between 15 and 85 mJy in an effort to characterize the effect of lensing across the entire million-source *Herschel* catalogue. These lensed candidates were identified by their close proximity to bright galaxies in the near-infrared VISTA Kilo-Degree Infrared Galaxy survey. Our high-resolution observations (0.15 arcsec) confirm 47 per cent of the initial candidates as gravitational lenses, while lensing cannot be excluded across the remaining sample. We find average lensing masses ($\log M/M_\odot = 12.9 \pm 0.5$) in line with previous experiments, although direct observations might struggle to identify the most massive foreground lenses across the remaining 53 per cent of the sample, particularly for lenses with larger Einstein radii. Our observations confirm previous indications that more lenses exist at low flux densities than expected from strong galaxy–galaxy lensing models alone, where the excess is likely due to additional contributions of cluster lenses and weak lensing. If we apply our method across the total 660 square degree H-ATLAS field, it would allow us to robustly identify 3000 gravitational lenses across the 660 square degree *Herschel* ATLAS fields.

Key words: general – gravitational lensing: strong – galaxies: evolution – galaxies: high-redshift – submillimetre: galaxies.

1 INTRODUCTION

Concentrated mass distributions, such as stars (Dyson, Eddington & Davidson 1920; Kelly et al. 2018; Welch et al. 2022), galaxies (Treu 2010), and galaxy clusters (Kneib & Natarajan 2011; González-Nuevo et al. 2012, 2017; Bonavera et al. 2019; Crespo et al. 2022; Fernandez et al. 2022) can redirect light, extending the number of sightlines on to an object resulting in so-called gravitational lensing. Particularly in the case of strong gravitational lensing, defined as a magnification $\mu > 2$, these cases can offer a significant increase in spatial and observational sensitivity. This effect is determined by the foreground distribution of matter, and can thus provide a constraint on the mass distribution of our Universe (Kochanek 1992, 1996; Grillo, Lombardi & Bertin 2008; Oguri et al. 2012; Eales 2015).

Especially given the low angular resolution of submillimetre (sub-mm) observations, the increase in angular resolution by gravitational lensing resulted in spectacular images of dust-obscured

star formation at cosmic noon (ALMA Partnership et al. 2015; Dye et al. 2015; Rybak et al. 2015; Tamura et al. 2015). Initial observations in the late 1990's had revealed a population of dust-obscured galaxies rivalling the total galaxy evolution seen in optical wavelengths (Smail, Ivison & Blain 1997; Hughes et al. 1998; Ivison et al. 1998). The brightest dusty star-forming galaxies (DSFGs) have observed star-formation rates in excess of 1000 $M_\odot$ yr^{-1}, resulting in an unsustainable evolutionary phase through violent star-formation feedback (Andrews & Thompson 2011; Rowan-Robinson et al. 2016). The evolutionary pathway of these star-forming systems is still not adequately understood, as demonstrated by the prevalence estimates from DSFG models, which often predict three to four orders of magnitudes below what is observed (Baugh et al. 2005). Because these galaxies are very rare (a few per deg^2), hydrodynamical models struggle to include enough volume to simulate these galaxies accurately in order to test the evolutionary pathways of these DSFGs (e.g. Narayanan et al. 2015). As a consequence, the best path to understand DSFGs is through direct observations of complete samples. Gravitational lensing offers an opportunity to study these DSFGs at high resolution. Meanwhile, observations to date have revealed a large source-to-source variation, with some

★ E-mail: tom.bakx@chalmers.se

sources showing stable rotation (Dye et al. 2018; Rizzo et al. 2020), while other sources appear to be in a state of rapid collapse (e.g. SDP.81, Dye et al. 2015; Rybak et al. 2015; Tamura et al. 2015). In order to capture this large variation of sources, large samples (>100) of lensed DSFGs are needed to characterize the evolutionary pathway(s) of these extreme star-forming systems.

Although lensing is a rare phenomenon, large-area surveys in sub-mm and mm revealed a large population of ultra-bright sources, that upon further inspection were revealed to be gravitationally lensed (Negrello et al. 2010; Vieira et al. 2013; Negrello et al. 2014, 2017). The steep bright-end of the luminosity function (i.e. brighter sources are increasingly rare, Lapi et al. 2011) means that the unlikely gravitational lensing magnification of fainter but more numerous sources are statistically preferred to observing non-lensed intrinsically hyperluminous sources. As a result, in the sub-mm domain, the wide-field H-ATLAS (Eales et al. 2010) and HerMES (Oliver et al. 2012) surveys with the *Herschel Space Observatory* have revealed a population of dusty lensed sources by selecting sources at $S_{500} > 100$ mJy (Negrello et al. 2010). Similarly, the large-area nature of cosmic microwave background studies with ground- and space-based telescopes means that these surveys are also well-suited towards lens selection, with the all-sky *Planck* survey showcasing exceptional lensing morphologies (Kamieneski et al. 2023), and perfectly circular Einstein rings shown in the *South Pole Telescope* survey – revealed in high resolution with ALMA and JWST (Spilker et al. 2016; Rizzo et al. 2020). Finally, while the mapping speed of ground-based observations at sub-mm wavelengths is limited by the atmospheric transmission, the recent large-area SCUBA-2 Large eXtragalactic Survey is bridging the border between lenses and intrinsically bright sources (Garratt et al. 2023). The large beamwidth of these selection techniques, however, means that only time-expensive follow-up observations of these sources can reveal the true nature of these galaxies (Bussmann et al. 2013, 2015; Spilker et al. 2016) – and worse yet, the intrinsic properties of the sample as a whole (Gruppioni et al. 2013).

One way to circumvent these limitations is by a search for the foreground lensing systems at complementary wavelengths such as optical or near-infrared (NIR). These foreground galaxies might be detected in optical (SDSS, González-Nuevo et al. 2012, 2017, 2019; Bourne et al. 2016) or NIR [e.g. VISTA Kilo-Degree Infrared Galaxy survey (VIKING), Fleuren et al. 2012; Bakx, Eales & Amvrosiadis 2020a; Ward et al. 2022] surveys, while the dusty nature of these DSFGs mean the background galaxies are likely not detected in optical/NIR surveys. These tests vary in their sophistication, with several models simply identifying nearby foreground galaxies (Ne-grello et al. 2010; Roseboom et al. 2010), to innovative mathematical techniques (Fleuren et al. 2012; Bourne et al. 2016) and statistical correlations accounting for redshifts and spatial distributions (González-Nuevo et al. 2019), even including the additional spatial offsets due to gravitational lensing (Bakx, Eales & Amvrosiadis 2020a).

These methods can statistically characterize the prevalence of lensed sources across the full extent of the *Herschel* sample – near 1 million dusty sources (Valiante et al. 2016; Furlanetto et al. 2018; Maddox et al. 2018; Shirley et al. 2021; Ward et al. 2022) – however, they have not been tested experimentally. The best way of resolving gravitational lensing directly is through resolved sub-mm observations to reveal the lensing structures (Spilker et al. 2016; Amvrosiadis et al. 2018; Dye et al. 2018; Kamieneski et al. 2023). While the easiest lenses to identify are at the brightest flux densities (>100 mJy at 500 micron, Negrello et al. 2010, 2014, 2017), both in

terms of their apparent brightness and their likelihood to be lensed, the bulk of the *Herschel* population – and thus also the lenses – reside at the lower flux densities (20 mJy > S_{500} > 40 mJy). A thorough test of the fidelity of a lens-selection method should thus focus on these low-flux density sources.

In this paper, we report on the observation of 86 galaxies selected using a method based on a VIKING (+ KiDS)-based analysis from Bakx, Eales & Amvrosiadis (2020a). In Section 2, we describe the selection method. Section 3 details the observations, and Section 4 describes the implications of this survey on lenses within *Herschel* samples. We conclude in Section 5. Throughout this paper, we assume a flat Lambda cold dark matter cosmology with the best-fitting parameters derived from the *Planck* results (Planck Collaboration VI 2020), which are $\Omega_m = 0.315$, $\Omega_\Lambda = 0.685$, and $h = 0.674$.

2 LENS IDENTIFICATION AND SAMPLE SELECTION

In this section, we describe the method for finding lenses through combined NIR and far-infrared surveys, as well as the selected galaxies for this pilot survey.

2.1 Lens identification

The lens identifying method is based on finding a VIKING galaxy which is statistically likely to be associated with a *Herschel* source. As a further requirement, the presumed foreground source should be at a lower redshift than the estimated redshift of the sub-mm source – estimated from the sub-mm colours of the source (Pearson et al. 2013; Bakx et al. 2018) – and is therefore highly likely to be a lens (Bakx, Eales & Amvrosiadis 2020a). The standard statistical way of finding associated sources is by finding galaxies close enough to the *Herschel* positions that they are unlikely to be there by chance (Bourne et al. 2016). Our new method relies on the fact that most high-redshift (z > 2) sub-mm galaxies are not bright enough to be detected on wide-area optical and NIR surveys such as SDSS and VIKING (Wright et al. 2019), and so any galaxy that is close to the *Herschel* position on these images could likely be the lens (González-Nuevo et al. 2017), although a subset of DSFGs may not be NIR-faint (González-Nuevo et al. 2012). The statistical tool used for identifying lenses is called the likelihood estimator (Sutherland & Saunders 1992). This likelihood estimator calculates an individual so-called likelihood of an association of a NIR source close to a *Herschel* source given the magnitude distribution of the NIR magnitude and spatial offset. The likelihood reflects how unlikely each NIR–*Herschel* couple is through a measure of how many similar fields one would need to see before encountering a single one of these associations. The likelihood, L, of lensing candidates is often in excess of several hundreds or thousands, and is calculated as follows:

$$L = \frac{q(m)f(r)}{n(m)}. \tag{1}$$

In this equation, $q(m)$ represents the probability distribution of genuine counterparts at a magnitude m, $n(m)$ represents the background surface density distribution of unrelated objects (in units of arcsec^{-2}), and $f(r)$ represents the distribution of offsets between sub-mm and NIR positions produced by both positional errors between both catalogues and gravitational lensing offsets (in units of arcsec^{-2}; see Bakx, Eales & Amvrosiadis 2020a).

In order to arrive at a single probability – here called the reliability (R_j) – the likelihoods of each nearby NIR source are added together,

and include the possibility of the foreground source being too faint to be detected in the VIKING survey (i.e. $Q_0 = 0.82$, Fleuren et al. 2012; Bourne et al. 2016; Bakx, Eales & Amvrosiadis 2020a):

$$R_j = \frac{L_j}{\sum_i L_i + (1 - Q_0)}. \qquad (2)$$

In this equation, the reliability of each potential match, j, is calculated from the sum of the likelihoods of all nearby matches ($\sum_i L_i$) and the possibility that the foreground source is too faint to be detected. Bakx, Eales & Amvrosiadis (2020a) have found that the SDSS also misses about half the lenses, so an essential part of our method is that the search for the lens is carried out in the K_S band in the VIKING survey, where the lens (often a massive 'red-and-dead' elliptical) is virtually always bright enough to be detected (Bakx, Eales & Amvrosiadis 2020a). On top of this, unlike other methods for finding associated sources, we calibrated our statistical estimator on a sample of gravitationally lensed galaxies: the *Herschel bright sources* (Bakx et al. 2018, 2020b). This resulted in the insight that the angular distribution of lensed galaxies is not simply described by a Gaussian distribution, but instead requires a distribution that accounts for an additional offset due to galaxy–galaxy and galaxy–cluster lenses. The likelihood estimator does introduce biases in the types of lenses we can find. The VIKING survey is deep enough to detect most lensing galaxies ($M_* > 10^8\,M_\odot$). Meanwhile, the radial probability distribution is non-zero out to ≈ 10 arcsec, allowing us to find most cases of galaxy–galaxy lensing (<10 arcsec, Amvrosiadis et al. 2018). We do note, however, that the method becomes increasingly less sensitive towards larger offsets between the lensed galaxy and the deflector.

2.2 The FLASH sample: faint lenses found through associated selection from *Herschel*

This survey is based on the H-ATLAS 12-h equatorial field (Eales et al. 2010; Valiante et al. 2016), which has good coverage with the VIKING NIR and the optical KiDS survey. This field contains 35 512 *Herschel* sources. The radio NRAO VLA Sky Survey (NVSS) was used to remove blazars from the sample. A total of 350 H-ATLAS sources fall within 10 arcsec of an NVSS source, i.e. within the typical combined angular precision of *Herschel* (~ 2 arcsec) and NVSS (~ 7 arcsec). Here, we note that this step could also remove bright DSFGs in our sample, which is not an important drawback, since we are mostly interested in the fainter DSFGs, and here choose sample purity over completeness. The photometric redshifts of the H-ATLAS sources is then estimated by fitting a modified blackbody spectral energy distribution (SED) to the 250, 350, and 500 μm fluxes (Pearson et al. 2013; Bakx et al. 2018). Subsequently, we impose a redshift cut for all H-ATLAS sources, demanding $z_{phot} > 2.0$. These sources were then passed through the counterpart analysis of Bakx, Eales & Amvrosiadis (2020a), which identifies counterparts on the VIKING K_S-band images that are likely to be statistically associated with the *Herschel* sources. This uses a standard likelihood estimator (Sutherland & Saunders 1992; Fleuren et al. 2012; Bourne et al. 2016; Bakx, Eales & Amvrosiadis 2020a), which provides a probability for a VIKING counterpart to be genuine. A total of 7 362 GAMA-12 *Herschel* sources have nearby VIKING counterparts, no nearby NVSS radio sources, and lie above $z_{phot} > 2$. Wright et al. (2019) have used the nine photometric bands of VIKING and KiDS to produce photometric redshifts and stellar masses for the objects detected in the surveys. By comparing these redshift estimates and their errors, in combination with the photometric redshifts for the sub-mm sources and their errors [assuming $\Delta z = 0.13(1 + z)$,

Pearson et al. 2013], we identify the systems for which there was only a 0.1 per cent chance ($\sim 3.1\sigma$) that the *Herschel* source and the potential counterpart are actually at the same redshift, for a total of 6823 sources. In order to test the evolution of the lensing probability with *Herschel* flux density, we identify the most likely sources to be gravitationally lensed across a wide 500 μm flux density range, selecting towards the highest reliabilities within each 10 mJy flux density region that can be observed in a single observation by ALMA. In order to efficiently observe these sources, we require each source to be within 10 degrees from a single phase-centre to observe all targets within a minimum number of Scheduling Blocks. Above 40 mJy, fewer sources could be found in a single field that would be reliable candidates for gravitational lensing, and as a result most of the sources have S_{500} between 20 and 40 mJy. As a consequence of the dearth of likely lensed sources at the higher fluxes, several sources have stand-out properties such as large angular separations or lower reliabilities. We list the catalogue in Table 1, and show the redshift against the 500 μm flux in Fig. 1. The sources are sorted from lowest S_{500} to highest.

2.3 The statistics of the FLASH selection

Although these sources are the most likely gravitationally lensed candidates with $S_{500} = 10$–90 mJy, with very high individual probabilities, the large parent sample implies that there is a possibility for chance encounters. In an example as to why this is the case: Even if there were no true lensing candidates, the size of our sample would by chance pick up sources as lensing candidates. Fig. 2 shows a schematic overview of the FLASH source selection, starting from a perfect understanding of lensed (a) and non-lensed sources (b). The photometric selection ($z_{phot} > 2$) reduces the fraction of lensed and non-lensed sources with F_{ZL} and F_{ZN}, respectively. The subsequent cross-identification and removal of sources that are likely at the same redshift reduces the fraction by an additional F_{KL} and F_{KN}, respectively. The sources can then be placed in four different categories according to a confusion matrix proportional to

$$
\begin{aligned}
\text{true positives} \quad &= W \quad = a F_{ZL} F_{KL}, \\
\text{false positives} \quad &= X \quad = b F_{ZN} F_{KN}, \\
\text{false negatives} \quad &= Y \quad = a(1 - F_{ZL} F_{KL}), \text{ and} \\
\text{true negatives} \quad &= Z \quad = b(1 - F_{ZN} F_{KN}).
\end{aligned}
$$

The objective of these ALMA observations is to identify the true-positive sources, W, although it is not clear how many false positives are included in the FLASH selection. The ALMA observations will be able to identify the lens candidates from the sample, and provide a measure of $f_{ALMA} = W/(W + X)$. Rewriting this equation, we find

$$f_{ALMA} = \frac{a}{a + Q^{-1}b}, \qquad (3)$$

with Q a representative of the quality of our FLASH selection,

$$Q = \frac{F_{ZL} F_{KL}}{F_{ZN} F_{KN}}. \qquad (4)$$

This allows us to find a rough estimate for the number of lenses we can expect to detect with these ALMA observations. The lensing fraction of sources decreases dramatically with decreasing flux density, which thus drives up the false-positive fraction at the lower fluxes. For instance, the lensing fraction predicted from cosmological models (Cai et al. 2013) suggest that only 1 per cent to 2 per cent of $z > 2$ sub-mm sources is lensed at $S_{500} = 30$ mJy, i.e. $a/(a + b) = 0.01$–0.02. The selection effects of the cross-identification is roughly

Table 1. FLASH catalogue.

Name	Herschel position	$S_{250\mu m}$	$S_{350\mu m}$	$S_{500\mu m}$	$z_{phot, sub-mm}$	VIKING position	θ	$z_{phot, VIK}$	K_S	LHR	M_*
	(hms dms)	mJy	mJy	mJy		(hms dms)	(arcsec)		mag_{AB}	(0–1)	$M_\odot$
FLASH-1	12:14:36.2−01:24:06.9	23.0 ± 5.9	32.4 ± 7.4	12.2 ± 7.7	2.08	12:14:36.2−01:24:06.3	0.93	$0.84^{+0.03}_{-0.04}$	18.87 ± 0.02	0.997	11.21
FLASH-2	11:36:31.9+00:40:21.7	30.8 ± 7.5	42.5 ± 8.1	19.7 ± 8.7	2.18	11:36:31.9+00:40:21.8	0.16	$0.75^{+0.11}_{-0.05}$	20.63 ± 0.10	0.997	10.07
FLASH-3	11:46:51.9−00:00:44.1	24.6 ± 6.1	18.4 ± 7.4	19.8 ± 7.8	2.18	11:46:51.9−00:00:45.1	0.97	$1.1^{+0.12}_{-0.05}$	20.26 ± 0.05	0.995	11.05
FLASH-4	11:54:08.8−01:44:16.1	33.2 ± 7.4	34.5 ± 8.2	20.7 ± 8.7	2.01	11:54:08.8−01:44:16.6	0.57	$1.25^{+0.20}_{-0.13}$	20.75 ± 0.12	0.995	10.95
FLASH-5	12:21:23.7+00:28:34.7	28.7 ± 7.3	33.9 ± 8.2	21.9 ± 8.8	2.32	12:21:23.6+00:28:35.9	1.96	$1.33^{+0.03}_{-0.03}$	18.94 ± 0.03	0.991	11.18
FLASH-6	12:16:56.5−02:37:41.2	29.0 ± 7.3	39.1 ± 8.2	22.2 ± 8.5	2.36	12:16:56.5−02:37:41.9	0.67	$0.63^{+0.04}_{-0.05}$	20.60 ± 0.11	0.995	9.677
FLASH-7	11:59:32.4+00:02:17.9	21.3 ± 5.7	32.7 ± 7.4	22.3 ± 7.7	2.91	11:59:32.4+00:02:17.9	0.36	$0.19^{+0.03}_{-0.04}$	20.24 ± 0.05	0.997	8.983
FLASH-8	12:19:11.4−00:30:36.9	29.4 ± 7.3	38.4 ± 8.0	22.4 ± 8.5	2.34	12:19:11.4−00:30:36.8	0.9	$1.31^{+0.04}_{-0.04}$	19.86 ± 0.06	0.995	10.72
FLASH-9	12:15:14.0−01:59:52.8	36.2 ± 7.0	39.9 ± 7.8	22.6 ± 8.2	2.04	12:15:14.0−01:59:52.3	0.76	$0.66^{+0.02}_{-0.04}$	18.76 ± 0.01	0.998	10.83
FLASH-10	11:45:49.3+00:20:38.0	27.6 ± 6.5	20.3 ± 7.5	22.8 ± 7.7	2.27	11:45:49.3+00:20:39.2	1.51	$1.28^{+0.05}_{-0.08}$	20.60 ± 0.07	0.99	10.67

Notes. Col. 1: Source name, sorted from lowest 500 μm flux to highest. Col. 2: RA and DEC positions in hms and dms units, respectively. Col. 3–5: The *Herschel* photometry. Col. 6: Photometric redshift of the *Herschel* source based on the fitting of the modified blackbody template from Pearson et al. (2013). Typical errors on this fit are on the order of 0.13(1 + z). Col. 7: The position of the VIKING-identified source from the catalogues described in Wright et al. (2019) Col. 8: The angular offset in units of arcsec between the *Herschel* and VIKING source. Col. 9: The photometric redshift of the VIKING source based on both VISTA and KiDS photometry best-fit (Wright et al. 2019). Col. 10: The AB-magnitude in the K_S-band photometry. Col. 11: The reliability (i.e. the probability of the *Herschel* and VIKING sources to be associated. Note that this does not account for the inclusion of false positives in a large-area survey. Col. 12: The stellar mass estimate of the VIKING source identified from the KiDS and VISTA photometry, as described in Wright et al. (2019). This table is available in machine-readable form in the Supplementary Material.
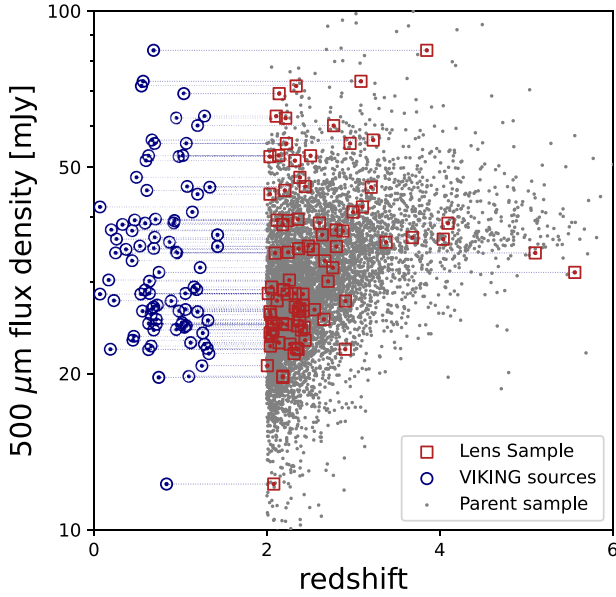
Figure 1. The photometric redshift distribution of the foreground (blue circles) VIKING and background (red squares) *Herschel* sources. The $z > 2$ *Herschel* sources from the equatorial GAMA 12 field are indicated in grey small points. We link the associated points together with a blue dashed line. The redshift difference between the sources provides confidence in being different galaxies (or not the same galaxy) as the *Herschel* sources.

$F_{KL} = 0.82$ (Bakx, Eales & Amvrosiadis 2020a), under the assumption that there are no systematic differences between the brighter lens samples (i.e. $S_{500} > 80$ mJy) and the bulk of lenses in *Herschel*. This is in line with a brief comparison of the equatorial sources reported in both Negrello et al. (2017) and Bakx, Eales & Amvrosiadis (2020a): For eight sources in the lensed sample of Negrello et al. (2017), seven are strong lensing candidates in Bakx, Eales & Amvrosiadis (2020a), or a $F'_{KL} = 0.88 \pm 0.12$. The fraction of lower redshift lenses excluded ($z < 2$) can be estimated from the fraction of such sources documented in Negrello et al. (2017). They report 15 out of 80 lens candidates to have photometric redshifts below 2, or $F_{ZL} = 0.82$. By comparing the photometric redshifts of the *Herschel* catalogues (Valiante et al. 2016; Furlanetto et al. 2018), we find that around 46 per cent of sources in a flux-limited ($S_{500} > 15$ mJy) sample lie below $z < 2$; i.e. $F_{ZN} = 0.54$. The main uncertainty of the method lies in our ability to remove false positives through the cross-identification analysis (Bakx, Eales & Amvrosiadis 2020a). As a lower limit, we can use the fact that *Herschel* and VIKING sources are excluded to be at the same redshift by $F_{KN} < 0.001$, although there are no direct measurements of F_{KN} possible without observations. For an intrinsic lensing fraction of $a/(a + b) = 0.01$, we can expect a high lensing fraction of $f_{ALMA} = 0.9$, and a Q value of 1250. We compare the sources in our sample against the lensing fraction predicted from cosmological models (Cai et al. 2013), and find a total of 82 out of 86 sources are likely lensed based on the above predictions.

The method further provides insight in the total number of lenses in the *Herschel* samples. The completeness of the sample, C, is equal to the number of lenses our method is able to identify among all true lenses,

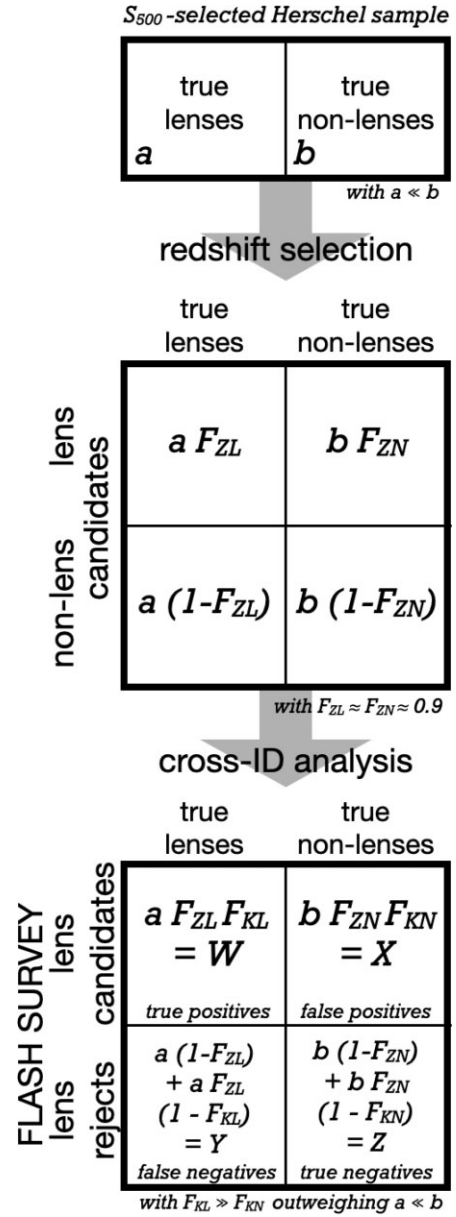$$C = \frac{W}{W + Y} = F_{KL}F_{ZL}. \tag{5}$$

Figure 2. A schematic overview of the FLASH source selection provides insight in the total number of expected lenses in the FLASH sample and the total number of lenses in the *Herschel* sample. True lenses and non-lenses are initially classified by a redshift cut ($z > 2$), followed by the cross-identification analysis (Bakx, Eales & Amvrosiadis 2020a) and a 3.1σ redshift difference between VIKING and *Herschel* sources. The subsequent confusion matrix contains a measure for the true positives, the additional false positives, and the completeness of the FLASH method.

As a result, an initial estimation of the completeness of the FLASH selection is around $C \approx 0.82 \times 0.8175 \approx 0.7 \pm 0.1$.

Fig. 3 shows the distribution of properties of the FLASH sources. Unlike previous studies of gravitational lenses that focus on $S_{500} > 100$ mJy (Negrello et al. 2017, or equivalent fluxes at longer wavelengths, Vieira et al. 2013; Spilker et al. 2016; Harrington et al. 2021; Kamieneski et al. 2023), this survey selects relatively low 500 μm fluxes. The reliability, or the statistical association of the *Herschel* sources to VIKING galaxies, of these sources is high due to a combination of low angular separation and bright
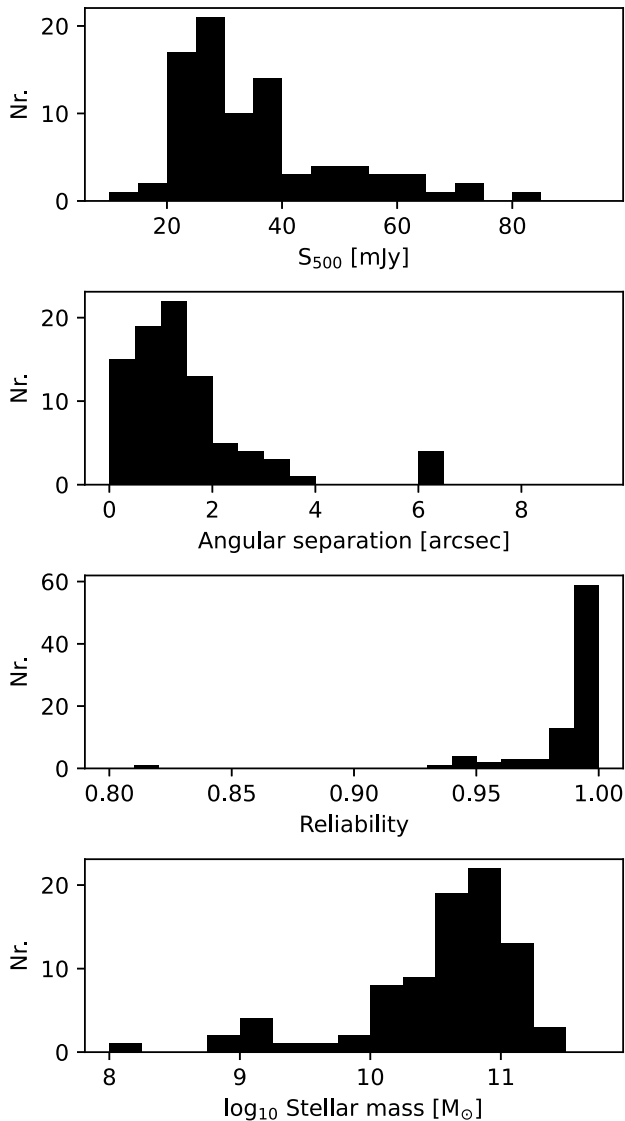
Figure 3. The FLASH sources are selected with *faint* 500 μm flux densities, relative to the bulk of the lenses found by *Herschel* and other lensing surveys (i.e. the expected or observed S_{500} of *Planck*, South Pole Telescope, and Atacama Cosmology Telescope are >100 mJy). They are found close to bright VIKING sources, with most *Herschel* and VIKING sources only 2 arcsec removed from on the sky, within the typical astrometric uncertainties. As a result of the close location on the sky, the FLASH sources have high reliabilities (i.e. association probabilities) for each *Herschel* and VIKING-association, with most association probabilities above the 99th percentile. The foreground VIKING sources have information from both VISTA (*Z*, *Y*, *J*, *H*, and K_S) and from the KiDS survey (*u*, *g*, *r*, and *i*). Spectral fitting (Wright et al. 2019) provides a stellar mass estimate of the foreground objects, which suggests massive ($M_* > 10^{10}$ M$_\odot$) galaxy systems at lower redshifts. Interestingly, each distribution appears to have one to three *straggling* sources with a large separations (≈6 arcsec; FLASH-39, -83, and -84), a low reliability ($R \approx$ 0.8; FLASH-79), or a low stellar mass ($M_* \approx 10^{7.8}$ M$_\odot$; FLASH-67), although each such source is different, and it does not suggest impurity of the sample.

foreground galaxy selection. The angular separation is on the order of the typical astrometric uncertainties (e.g. Valiante et al. 2016). In fact, most association probabilities of FLASH sources are above the 99th percentile. The foreground VIKING sources have information from both VISTA (*Z*, *Y*, *J*, *H*, and K_S) and from the KiDS survey (*u*, *g*, *r*, and *i*). Spectral fitting (Wright et al. 2019) provides a stellar

mass estimate of the foreground objects, which suggests massive ($M_* > 10^{10}$ M$_\odot$) galaxy systems at lower redshifts. As previously mentioned, the sample is drawn from a relatively small patch of sky to facilitate efficient ALMA observations. As a consequence, each distribution appears to have one to three outliers source with a large separations (≈6 arcsec; FLASH-39, -83, and -84), a low reliability ($R \approx$ 0.8; FLASH-79), or a low stellar mass ($M_* \approx 10^{7.8}$ M$_\odot$; FLASH-67), although each such source is different, and do not suggest impurity of the sample.

3 ALMA OBSERVATIONS, REDUCTION, AND RESULTS

3.1 ALMA observations and reduction

We observe using Band 7 continuum observations to test whether these sources are actually lensed. The observation depth is based on a Cycle 2 ALMA program of 16 bright *Herschel* sources that showed that even short (2 min) continuum observations were enough to reveal the lensed structure with enough signal-to-noise and resolution for a full lensing reconstruction (Amvrosiadis et al. 2018; Dye et al. 2018). In this study (2019.1.01784.S; P.I. Bakx), we have used the same resolution (∼0.15 arcsec) but scaled the integration times to allow for the fainter flux densities of the sources by 50 per cent deeper observations (see Table 2). The quasars J1058+0133 and J1256−0547 were used as bandpass calibrators, and quasars J1217−0029 and J1135−0428 were used as complex gain calibrators.

Data reduction was performed following the standard procedure and using the ALMA pipeline. Then, we use CASA for imaging the *uv*-visibilities using Briggs weighting with a robust parameter of 2.0 (to maximize the depth of the observations at the expense of slightly increasing the final synthesized beam size). The resulting beam size is 0.″18 by 0.″14 with a beam angle of −71 degrees at a continuum depth of 72 μJy per beam.

In order to test the effect of resolved observations and to facilitate aperture extraction, we also generate images with a tapering of 0.5 arcsec. The resulting continuum maps have a beam size of 0.″60 by 0.″56 at the same beam angle of −71 degrees at a continuum depth of 137 μJy per beam.

3.2 ALMA photometry

The source fluxes are extracted from the tapered image using the CASA IMFIT routine. For each source, the routine is repeated until no obvious sources exist in the residual image ($>3\sigma$). The resulting positions and fluxes are shown in Table 3. For significantly sources or sources where the lensing causes the emission to be spread across multiple components, we mention the individual extracted positions, as well as the combined flux of the source. We indicate these sources with italics.

The resulting images are shown in Fig. 4. These images, whose identification and FLASH number are listed at the top, show the VIKING image in the background, with foreground contours from the high resolution (white contours) and tapered (solid black contours). Inset images provide the high-resolution (0.15 arcsec resolution; red contours) for sources where zoom-ins are necessary. The images are centred on the VIKING position (which is also the ALMA phase centre), and the orange cross indicates the *Herschel* position from Valiante et al. (2016). The red squares indicate the individual positions of the extracted fluxes.

Table 2. Parameters of the ALMA observations.

UTC start time [YYYY-MM-DD hh:mm:ss]	Baseline length (m)	N_{ant}	Frequency (GHz)	T_{int} (min)	PWV (mm)
2021-05-10 03:08:31	14–2492	44	343.484	49.0	0.96
2021-05-16 03:21:37	14–2517	47	343.484	48.8	0.96
2021-05-17 00:05:58	14–2517	47	343.484	48.9	0.65
2021-05-17 01:55:18	14–2517	48	343.484	49.0	0.64
2021-05-17 02:43:09	14–2517	48	343.484	21.8	0.45
2021-05-18 00:13:21	14–2517	49	343.484	42.3	0.62
2021-05-18 04:03:52	14–2517	49	343.484	42.3	0.39

3.3 ALMA observation completion

Several sources do not have bright emission in their reduced images. Notably FLASH-6 ($S_{500} = 22.2$ mJy) does not show any emission in the ALMA imaging. Here, we explore the reasons for these non-detections. The ALMA observations were centred on the VIKING position, in order to accurately probe the lensing structure expected around the foreground lens. The field of view (FoV) of ALMA is limited to ∼15 arcsec, however, and there exists the possibility of sources falling outside of the primary beam – although this is increasingly unlikely to be due to galaxy–galaxy lensing (Amvrosiadis et al. 2018).

Fig. 5 shows the observed offset between the ALMA-identified sources and the VIKING central source. The black line shows the 3σ detection limit based on the 0.5 arcsec tapered image used for source extraction. The majority of sources have detected emission within the FoV of ALMA, and importantly, the typical source flux lies a factor of two or more above the detection limit. However, the individual sources approach the end of the FoV of the Band 7 observations by ALMA, even though the selection towards large values of the reliability means that these sources have a small distance between the VIKING and *Herschel*-estimated position for the source. Even a shift of 5 arcsec – common across the sample – could push sources into a less sensitive part of the primary beam, and result in non-detections. The fact that lenses can be extended across the source further increases the detection threshold, further complicates this matter. On the whole, we have a large detection fraction for most sources, although current observations cannot exclude faint, extended, or cluster lenses to be completely accounted for in the ALMA observations.

4 LENSING IN *HERSCHEL* SAMPLES

In this section, we discuss the lensing nature of FLASH sources based on the ALMA images. Here, we differentiate obvious strong lenses, investigate more difficult sources which could be lensed or not lensed, and explore the effects of selection biases in the sample. Finally, we zoom out to the complete perspective of lenses to be found in the *Herschel* samples with the FLASH method.

4.1 Lensing nature of FLASH sources

The ALMA observations reveal a large spread in the observed morphologies (Fig. 4). Some *Herschel* sources are easy to visually identify as gravitational lenses, showing morphological features such as arcs, multiple images, and even near-complete Einstein rings. Other sources have multiple nearby counterparts, making interpretation of their lensing nature more difficult. These sys-

tems could be chance alignments, a situation where the *Herschel* source and VIKING galaxy are the same source, or cases of cluster lensing, where foreground clusters provide a speckled ALMA field with multiple sources, as well as the possibility of (proto)cluster environments where overdensities in the cosmic web are seen through an excess of ALMA sources. We summarize our knowledge on the lensing nature of each source by a grade ranging from A (secure lens identification) via B (some evidence for lensing) to C (no indications for lensing, or the lack thereof).

In brief, we identify A-grade lenses as sources where robust ALMA emission shows lensing features such as arcs or rings, or where the ALMA emission is between 0.2 and 2 arcsec removed from the central VIKING galaxy. B-grade sources consist of sources with emission either removed further than 2 arcsec – but morphologically appears to be consistent with lensing – or is within 0.2 arcsec of the VIKING galaxy – where we cannot exclude the ALMA observation of the VIKING galaxy. Sources without any of these features are categorized as C-grade. Below, the lens identification criteria are discussed in detail, and we summarize the results in Table 4.

4.1.1 Identifying lenses in FLASH

We investigate the lensing features of sources visually, identifying A-grade lenses by their extended or arced ALMA emission close to the central VIKING sources (i.e. <2 arcsec). These sources were selected with a small spatial separation between the *Herschel* and VIKING positions. The combined source-to-source angular separation of *Herschel* and VIKING sources, particularly at the lower significance levels, is on the order of 1 or 2 arcsec. For sources without obvious lensing features such as arcs or rings (e.g. FLASH-3), we interpret ALMA emission offset from the central VIKING source by more than 0.2 arcsec but less than 2 arcsec as indications of strong gravitational lensing. At these separations, the emission is likely not originating from the NIR emitting VIKING galaxy given the accurate photometry of ALMA and VIKING (<0.1 arcsec, Wright et al. 2019), but instead is lensed by the foreground source. On the other hand, if there exists bright VIKING emission at the position of the ALMA emission, we exclude the source as a lensing candidate, and award the source a B-grade. These provide us with a first-pass estimate of the number of A-grade lens candidates in the FLASH sample, for a total of 37 sources.

Since the sensitivity of our observations is not guaranteed to detect extended lensing features for all sources, we measure the curve of growth of ALMA emission through multiple annuli at different widths (0.15, 0.3, and 0.5). We calculate the signal-to-noise ratio for all pixels i within the annulus using the following equation:

Table 3. ALMA observations catalogue.

Name	Lens?	ALMA position (hms dms)	$S_{1.1mm}$ mJy	$\theta_{ALMA, VIK}$ (arcsec)	$\theta_{ALMA,Herschel}$ (arcsec)
FLASH-1NE	C-grade	12:14:36.9−01:24:03.0	$2.14 \pm 0.66\ (3.3\sigma)$	10.0	10.9
FLASH-1NW	...	12:14:36.7−01:24:11.7	$1.17 \pm 0.4\ (2.9\sigma)$	9.1	9.4
FLASH-2S	C-grade	11:36:31.5+00:40:22.4	$6.81 \pm 0.3\ (22.4\sigma)$	4.7	4.6
FLASH-2NW	...	11:36:32.3+00:40:14.5	$2.1 \pm 0.7\ (3.0\sigma)$	9.7	9.8
FLASH-3	A-grade	11:46:51.9−00:00:45.0	$0.96 \pm 0.19\ (5.0\sigma)$	0.3	1.0
FLASH-4E	B-grade	11:54:08.9−01:44:12.8	$2.13 \pm 0.32\ (6.7\sigma)$	3.9	3.3
FLASH-4C	...	11:54:08.8−01:44:16.6	$0.67 \pm 0.19\ (3.5\sigma)$	0.4	0.5
FLASH-4S	...	11:54:08.3−01:44:14.3	$1.72 \pm 0.58\ (3.0\sigma)$	8.2	7.9
FLASH-5E	C-grade	12:21:23.8+00:28:41.2	$1.83 \pm 0.4\ (4.6\sigma)$	6.2	6.7
FLASH-5W	...	12:21:23.3+00:28:28.2	$1.53 \pm 0.57\ (2.7\sigma)$	8.9	8.9

Notes. Col. 1: Source name. We identify the fluxes of the individually extracted fluxes (red boxes in Fig. 4), and for extended or lensed sources, we provide the total flux and weighted signal-to-noise ratios of the lensed components in the sources indicated with italics. The additional letters in the naming convention refer to N, E (left in figures), S, W (right in figures) for north, east, south, and west. C refers to centre, for sources closer to the centre than others. Col. 2: The identification of the source, as discussed in Section 4.1. Col. 3: The RA and DEC position of the ALMA positions in units of hms and dms, respectively. We do not provide the position for the combined lensed sources, as these do not represent any physical position. Col. 4: The 1.1 mm flux density followed by the signal-to-noise ratio of the detection in brackets. Col. 5: The angular offset between the ALMA and VIKING position in units of arcsec. Col. 5: The angular offset between the ALMA and *Herschel* position in units of arcsec. This table is available in machine-readable form in the Supplementary Material.

$$SNR = \sum_i \frac{S_i}{\sigma \sqrt{N_{pix} N_{beam}}}. \qquad (6)$$

In this explicit equation, the per-beam flux density, S_i (Jy per beam), is converted to the per-pixel flux density by dividing by the number of pixels per beam, N_{beam}. Subsequently, the per-pixel flux is summed over all pixels in the annulus, N_{pix} and is normalized to the per-field standard deviation, σ. The pixels are cross-correlated on the scale of a beam, so this standard deviation needs to be corrected by the square-root of the number of pixels per beamsize, as well as correct for the reduced uncertainty for the larger aperture, i.e. $\sigma/\sqrt{N_{pix} N_{beam}}$, resulting in a noise profile with a unit variance centred around zero.

Fig. 6 shows the annuli-based curve-of-growth analyses for the three sources where additional >5σ ring-like features were found below the ordinary detection threshold: FLASH-30, FLASH-34, and FLASH-75. These graphs show the 5.5 arcsec surroundings of the VIKING sources, and fit annuli with three different widths (0.15, 0.3, and 0.5 arcsec) in an effort to reveal lensing features. The bottom panels show the signal-to-noise ratio as a function of angular distance. Direct observations of lensing features is explicitly less sensitive to larger lensing arcs, and all these features indicate Einstein radii below 1 arcsec. Several more sources have ∼4σ, although deeper observations are necessary to confirm these sources to exclude false positives.

4.1.2 Confusion between foreground and background sources

Our source selection included a low probability (<0.1 per cent) of overlap between the redshift probabilities of VIKING galaxies and *Herschel* sources. However, without spectroscopic observations, both of the VIKING galaxies and *Herschel* sources, we cannot exclude the possibility of observing the same object in VIKING as in *Herschel*. Since these sources are selected from roughly 50 square degrees, our method could instead be an effective way for finding NIR bright DSFGs (to be VIKING-detected) with cold dust (resulting in a vast overestimation of the sub-mm photometric redshift).

While the main goal of the ALMA observations was to unravel the morphologies of these galaxies, the observations also offer spectral information on these sources. Given the spectral coverage, we could detect carbon monoxide (CO), atomic Carbon ([C I]), or atomic lines of galaxies in the sample, see Fig. 7. For most of these solutions, the uncertainty in the photometric redshift is too large to use just a single line for a robust redshift identification, particularly since several of these sources were extracted at low flux densities.

Using the tapered data cubes, we initially inspect the galaxies at the extraction position. These tapered data cubes are created by effectively down-weighing the long baselines of ALMA. This allows us to extract positions and fluxes with higher fidelity, since tapering results in higher significance detections at a moderate cost in resolution for resolved sources. After a visual inspection of the spectra, we perform per-source based aperture photometry to extract the emission line across the source.

In total, five sources show line emission at their ALMA position. We note that these are tentative spectroscopic redshift solutions, and require confirmation.

FLASH-28 (*A-grade*) has a line feature at 348 GHz, with an extension at 348.3 GHz. The source is identified as a gravitational lens, with an expected VIKING-lens redshift of $z = 0.9$–1.07. The background photometric redshift is $z_{sub} = 2.36$, and a potential redshift solution could be $z = 2.312$ from CO(10-9).

FLASH-33C (*C-grade*) has a line feature at 350.2 GHz. This source could be associated with the foreground VIKING source, and while the background redshift ($z_{sub} = 2.91$), the VIKING system has a photometric redshift of $z = 0.85$–0.93. The source is offset by 2.7 arcsec, and is likely not associated to the foreground system. The curve-of-growth analysis finds a ringed system surrounding FLASH-33, on top of the multiple components identified by direct imaging. It is thus likely that it is a background source at $z_{spec} = 2.62$ for CO(10–9) for example.

FLASH-49 (*A-grade*) has a line feature at 351 GHz. This ALMA-detected source, with $z_{sub} = 2.25$, is likely unrelated to the foreground VIKING source between $z = 0.91$ and 0.98 given its spatial offset. A potential solution would be the CO(10-9) line at redshift $z = 2.284$.
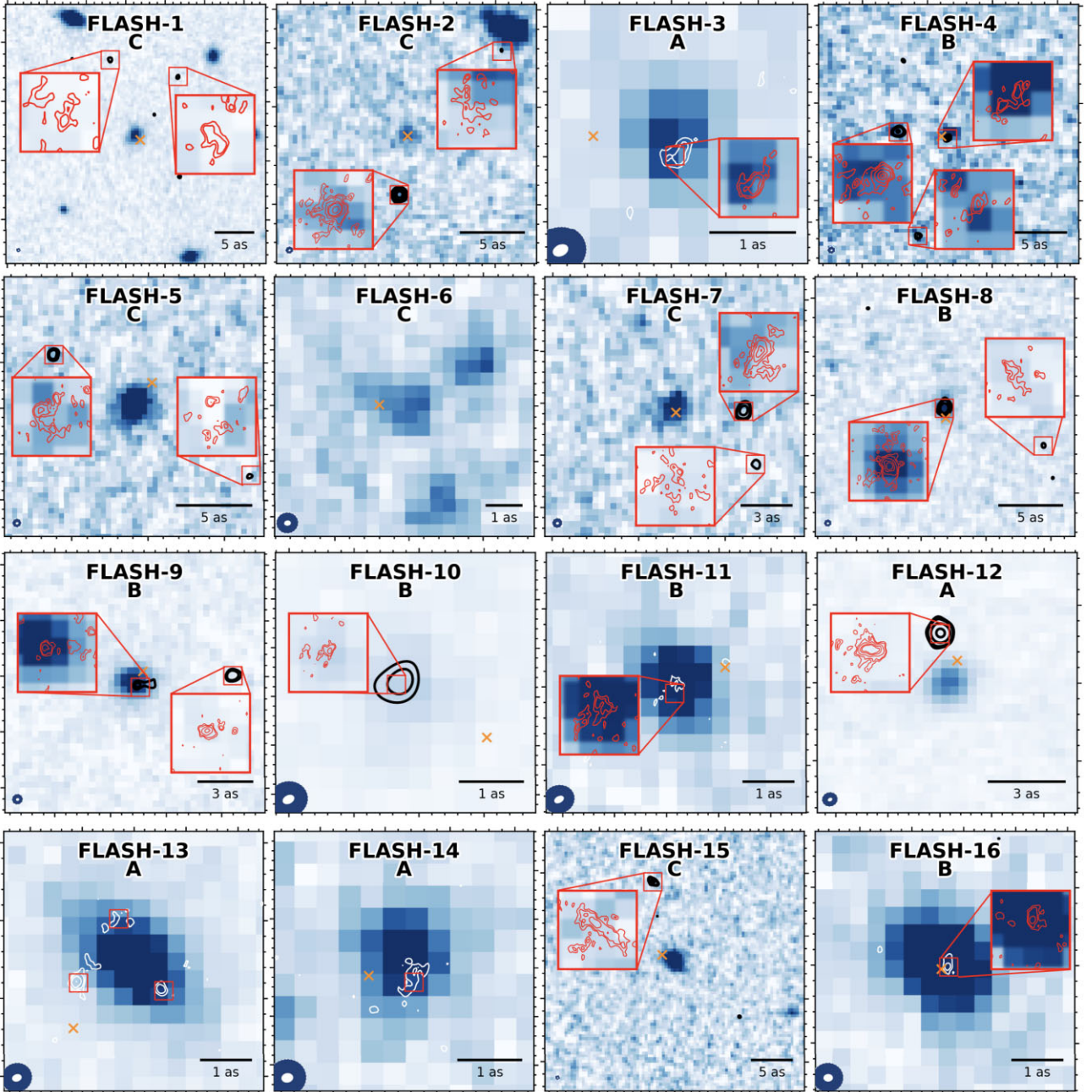
Figure 4. The VIKING images of the FLASH sources are shown in the blue background, with their FLASH number and identification listed in the top of the figure. Contours in the central panels show either the robust parameter $=2$ maps (white contours; beam ≈ 0.15 arcsec) or the tapered data (black contours; beam ≈ 0.55 arcsec). The contours are drawn at 3σ, 5σ, 8σ, 10σ, and 20σ. The beams are shown in the lower left of the panels, and the images are scaled to include all ALMA-identified galaxies. The angular scale is shown in the lower right of each figure in units of arcsec. The extraction positions of the sources in Table 3 are indicated with red boxes, and where applicable, we provide insets of each source using red contours on the scale to capture the entire emission. In order to boost the fidelity of these insets, we lower the contour levels to 2σ, 3σ, 5σ, 10σ, and 20σ. The images are centred on the VIKING-position, and the orange cross indicates the *Herschel* position. The FLASH numbering is sorted by increasing 500 µm flux, S_{500}.

FLASH-76W (*A-grade*) shows a line feature at 338.0 GHz with an additional feature at 339 GHz. The *Herschel* source is expected to lie at $z_{sub} = 2.14$, with the VIKING source between $z = 0.95$ to 1.13. The ALMA morphology suggests it is a lensed system, although no line emission was seen in the weaker counter-image. A potential redshift solution could be that these are the CO(7-6) and [C I](2-1) emission lines at $z = 1.387$. The fidelity of the second line is currently still too low to exclude any other solutions.

FLASH-86N (*A-grade*) shows an absorption feature at 336.2 GHz. The source at $z = 3.85$ is lensed by a foreground VIKING source between $z = 0.63$ and 0.73. The only bright absorption feature is the CH$^+$(2-1) absorption line, confirming its redshift to be $z = 3.965$.

Although four of these five sources had already been confirmed to be lensing systems through the visual identification methods, none of the five sources with line observations provide indications of confusion between the foreground and background source. At
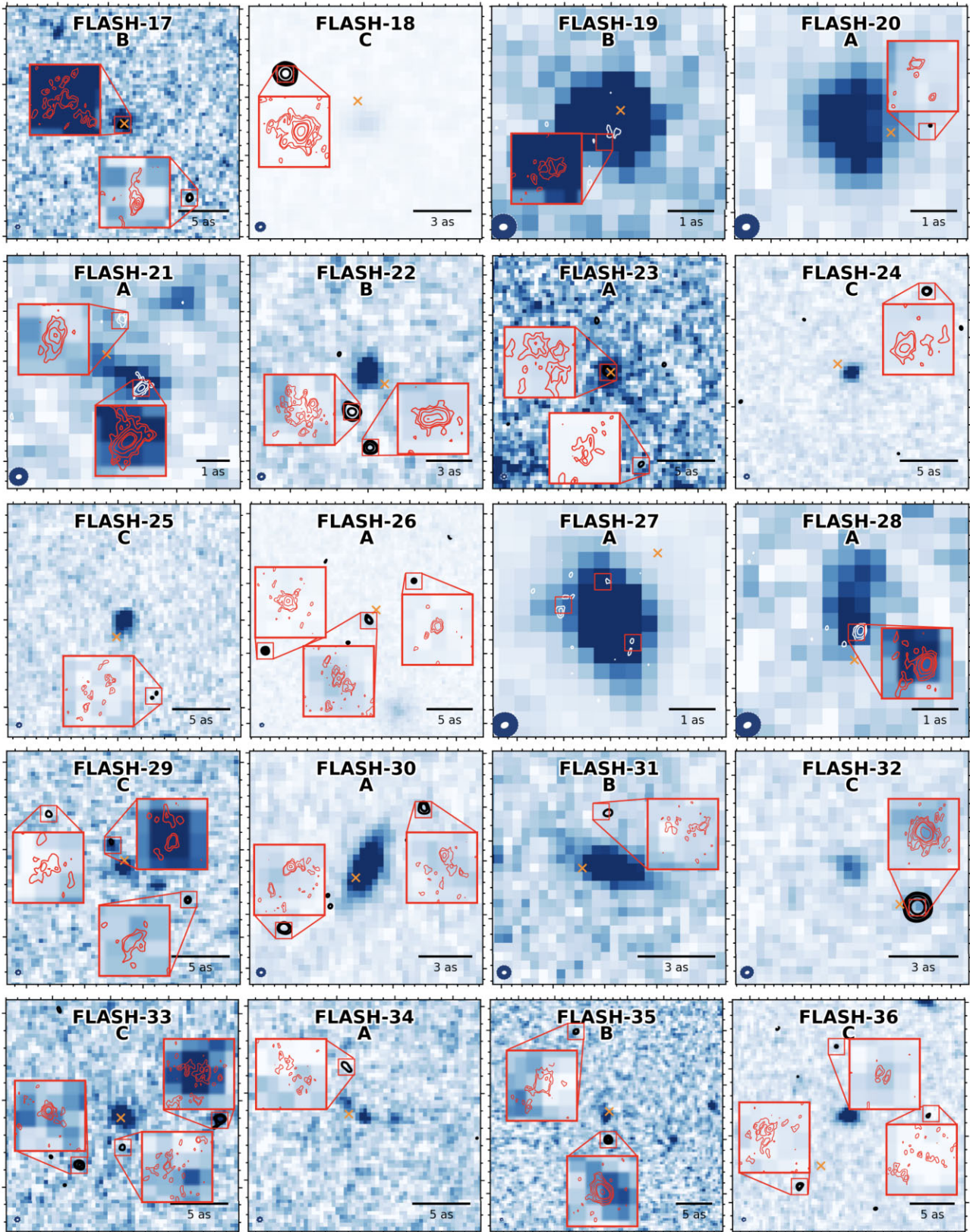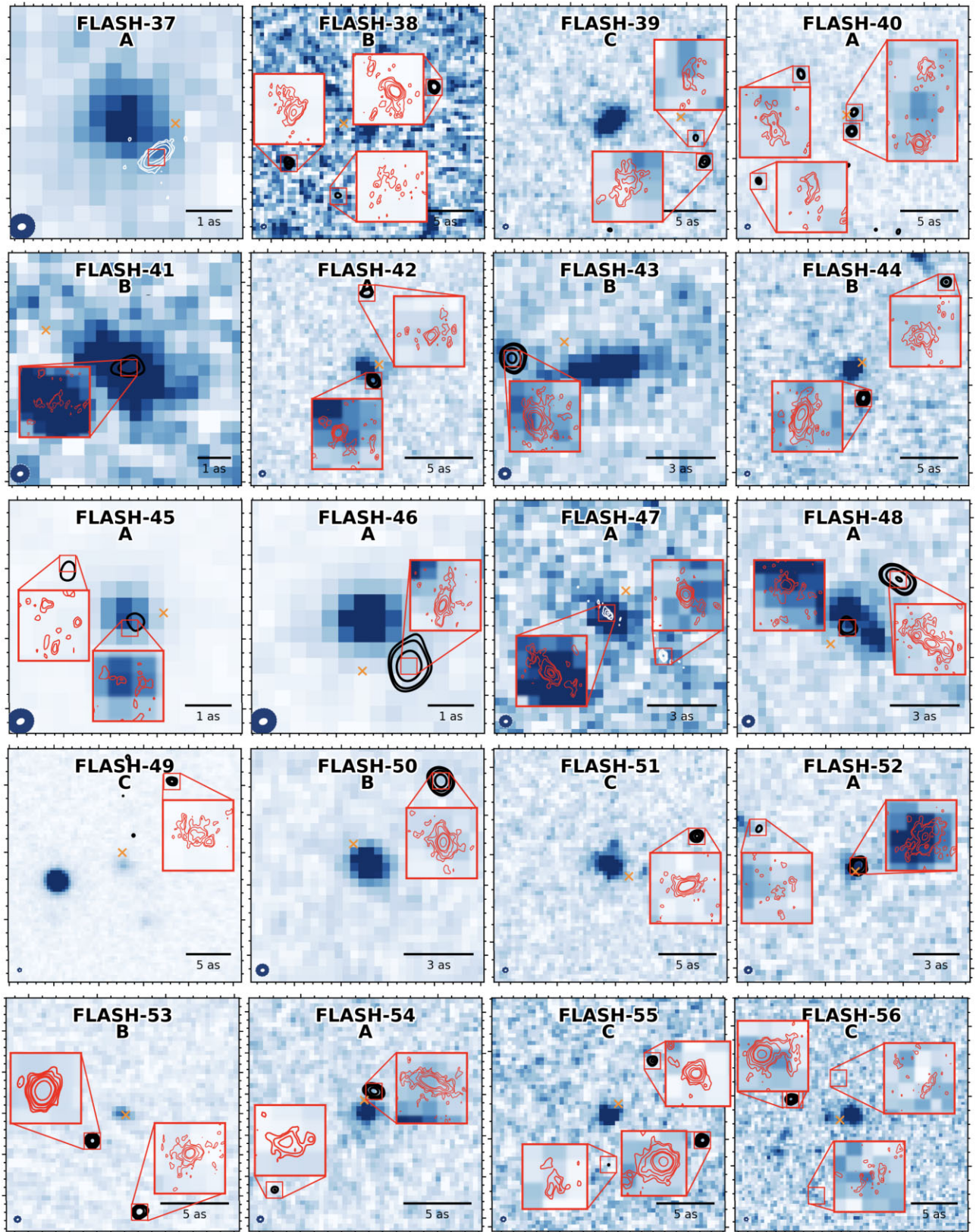
Figure 4. Continued.
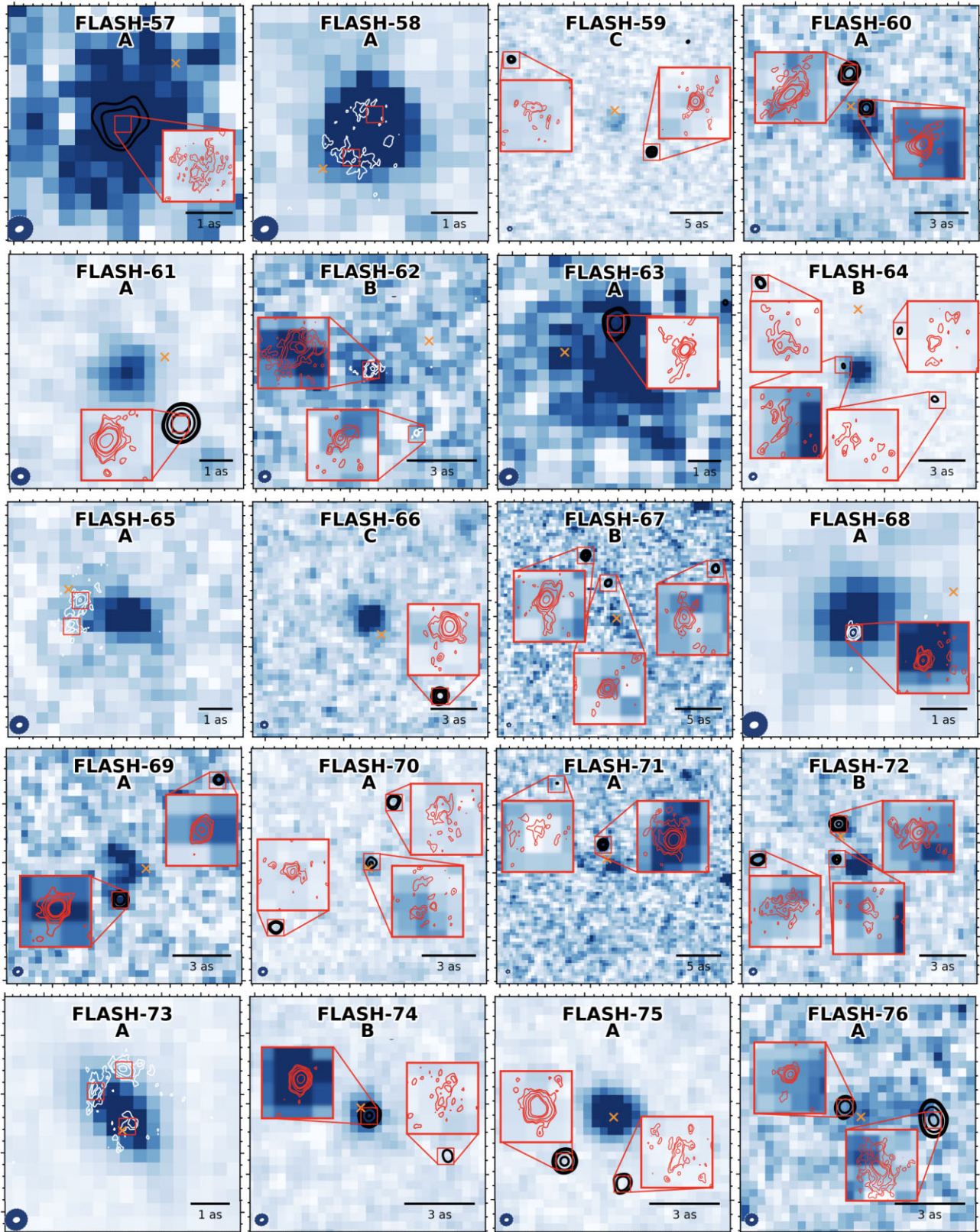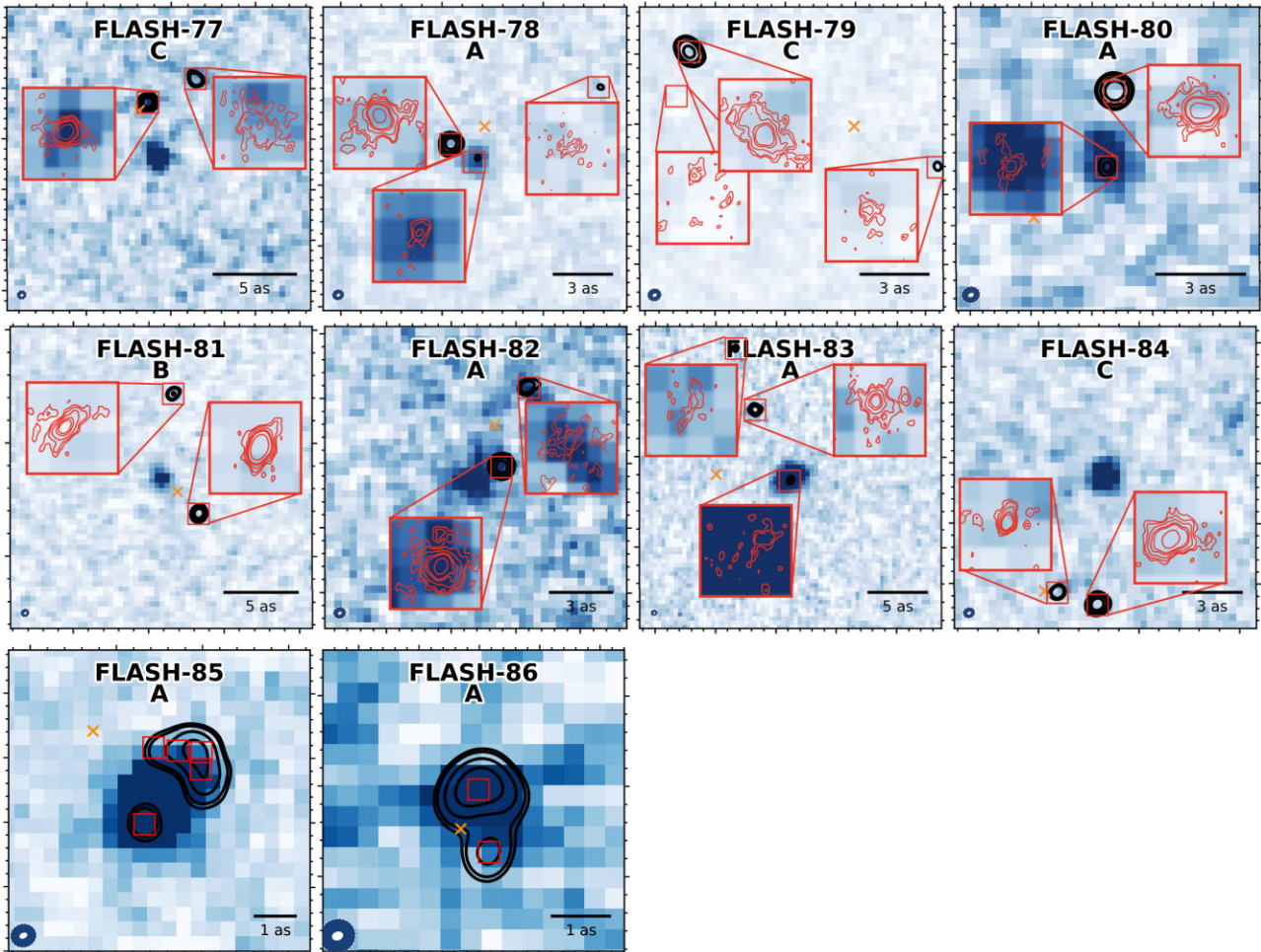
Figure 4. Continued.

Figure 4. Continued.

Figure 4. Continued.

least, this provides some confidence in the redshift cut between the foreground and background source.

In Fig. 8, we show the distribution of the photometric redshift difference between sources with different lensing classifications. Simplistically, the assumption could be that the confusion between foreground and background sources would show up as a lower average difference between the two sources. Instead, there does not appear to be a significant difference between the redshift difference of A-grade sources and the B- and C-grade classifications. There could thus be a small contribution of confusion between foreground and background systems, although so far there are no concrete indications from spectroscopy or from the redshift difference distributions. The redshift selection criterion in the selection technique appears robust.

4.1.3 Cluster lenses and protoclusters in the FLASH sample

The sources in the FLASH sample are selected from *Herschel* catalogues, which are extracted from the ≈18 arcsec-wide SPIRE 250 μm point spread functions. This has increased the possibility of *source confusion*, where multiple sources are confused as a single emitting source. While the FLASH sources are selected as singular *Herschel* sources, they could instead be resolved into multiple sources by ALMA. Particularly at fluxes of $S_{500} = 20$–40,

the confusion fraction can be around 40 per cent (Scudder et al. 2016) or higher (see Bendo et al. 2023 for a more complete discussion). Based on number counts from a hydrodynamical model by Lagos et al. (2020), about half of the fields is predicted to contain an additional emitter at 3σ, although the *Herschel* source pre-selection increases this probability. 47 fields contain more than one emitter (excluding multiple images from lenses), in line with the prediction from random pointings. This does not mean that there is no indication of excess sources. 16 fields contain more than two sources, of which FLASH-40 and -64 contain four ALMA sources, far above the expected number of fields with multiplicity. The FLASH-40 system has a A-grade lens, while FLASH-64 has a nearby source that could indicate a lensed galaxy, suggesting that source multiplicity is not the only driver of such sources, but that gravitationally lensed sources could also trace environments with multiple sources (Overzier 2016).

On the other hand, the foreground imaging from VIKING reveals around 12 fields with multiple NIR bright sources. Our selection method aims towards galaxy–galaxy lensing, but might also pick up galaxy–cluster lensing. Using a visual identification, we identify two A-grade sources (FLASH-21 and -82), five B-grade sources (FLASH-4, -35, -43, -44, and -62), and five C-grade sources (FLASH-1, -6, -29, -56, and -77) with additional bright VIKING galaxies. The grade identification relies on low angular separations, in line with high-magnification galaxy–galaxy lenses; however, our
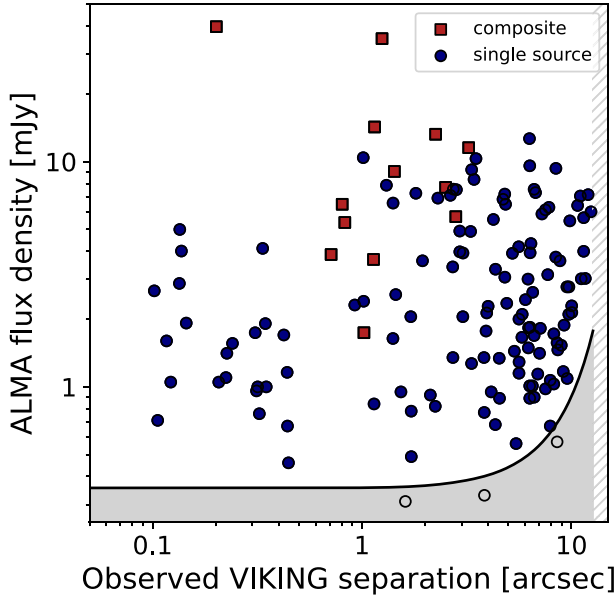
Figure 5. The observed ALMA flux densities (solid blue circles for single sources; red squares for composite sources, where composite sources are shown in italics in Table 3) are shown against the angular offset from the phase centre, i.e. the VIKING source position. The solid black line and fill indicate the ALMA primary beam sensitivity down to 3σ. The typical flux densities of the sources are higher than the observation depth. Although most sources are detected away from the edge of the ALMA beam, we cannot guarantee that sources could lie outside of the FoV. Similarly, several sources scatter below the detection threshold, and particularly since lensed sources could be extended, we cannot guarantee the sample observations are complete.

Table 4. The classification of FLASH sources.

S_{500} (mJy)	Nr.	A-grade (per cent)	B-grade (per cent)	C-grade (per cent)
10–25	21	29	33	38
25–35	30	43	30	27
35–45	17	53	24	24
45–55	8	75	0	25
55–65	6	50	33	17
65–75	3	67	33	0
75–85	1	100	0	0

Notes. Col. 1: The 500 μm flux bin. Col. 2: The number of sources contributing to each flux bin. Col. 3: The expected number of lenses based on the false-positive considerations in the sample selection (Section 2). Col. 4–6: The distribution of sources in each bin.

method might not be as good at identifying cluster lenses with larger separations, or galaxy–galaxy lenses with large separations and lower magnifications, perhaps in the range of weak lensing.

4.2 Effectiveness of the FLASH method

We robustly identify 40 lensed sources (A-grade), at 47 per cent of the total sample. In 23 cases, there are some tentative indications of lensing, which cannot be confirmed with current observations (B-grade). For the remaining 23 cases, the ALMA observations provide no indications of gravitational lensing (C-grade). Several stand-out sources show-case lensing in near-complete Einstein rings, such as FLASH-13, -27, -58, -73, -85, and -86 (see Appendix Fig. A1).

Particularly the lensing nature of FLASH-13, selected at a mere $S_{500} = 23.6$ mJy, confirms that our method is capable of selecting lenses at four or five times lower apparent flux densities than previous methods (Negrello et al. 2010, 2014, 2017; Vieira et al. 2013). Meanwhile, several A-grade sources do not have apparent counter-images in the ALMA observations, which could indicate weaker lensing below the strong-lensing regime of $\mu > 2$.

Fig. 9 shows the distribution of source types as a function of their flux density. Equation (3) predicted a high lensing fraction among the sample ($f_{\mathrm{ALMA}} = 0.9$); however, we are only able to confirm lensing for 47 per cent of sources (A-grade) through the ALMA observations. Meanwhile, the method appears to be most successful at the highest flux densities, as expected from previous lensing searches that focus on sources with a higher probability to be gravitationally lensed, such as Negrello et al. (2010).

The selection of foreground galaxies through VIKING could introduce a bias in the redshift selection. In Fig. 10, the redshifts of the foreground and background sources of each grade are shown against predictions from Lapi et al. (2012), Cai et al. (2013), and Eales (2015) for the foreground distributions. The models are dependent on the background source distribution. Here, we assume a lensed source redshift of $z_l = 2.5$, in line with the average redshift of our sample ($z_{l,\mathrm{FLASH}} = 2.5 \pm 0.6$). The redshift distribution of the foreground sources in FLASH is similar to the distributions predicted by the models, and there thus does not appear to be a preferential selection to either low- or high-redshift lenses in the FLASH method.

In Fig. 11, the reliability of each source is compared against their 500 μm flux density, highlighting the different nature of the sources accordingly. There does not appear to be a clear split in reliability between the C- and A-grade sources throughout the sample, with several C-grade sources at reliabilities $R \sim 0.995$. The effect of the false positives might thus be less than expected from previous work (Bakx, Eales & Amvrosiadis 2020a), which should increase rapidly for decreasing reliabilities. FLASH targeted the most likely lens candidates, and is representative of the sources with the highest reliabilities among the GAMA-12 sources, with reliabilities between 0.9 and 0.99.

The angular offset of the ALMA sources from the *Herschel* position is between 0.5 and 2 arcsec even for A-grade lens candidates. This indicates that one of the core ingredients in the lensing identification method, namely the angular offset, could be more uncertain than predicted. There thus exists an additional uncertainty in the likelihood ratio, resulting in scatter in the reliabilities of sources at the high end of the reliabilities. Instead, there could be a fundamental limit to the reliability of fainter sources, and consequently, there could be a certain level of false positives that statistical estimators for gravitational lenses are likely to include also in future works. The method from Bakx, Eales & Amvrosiadis (2020a), as well as other methods such as SHALOS (González-Nuevo et al. 2019), offer the ability to include the effect of additional angular offset; however, it is likely that the highest reliability sources ($R > 0.99$) will always be those scattered close to the nearby VIKING source. Conversely, the ability of this method to select lenses even at lower reliabilities suggests that it is useful to target lower reliability sources, enabling large lens samples in the near future.

4.3 The lensed galaxies of the FLASH sample

The properties of a galaxy–galaxy lensing event are described perfectly in the geometric terms of general relativity, as a function of the distances between the foreground and background galaxy, their
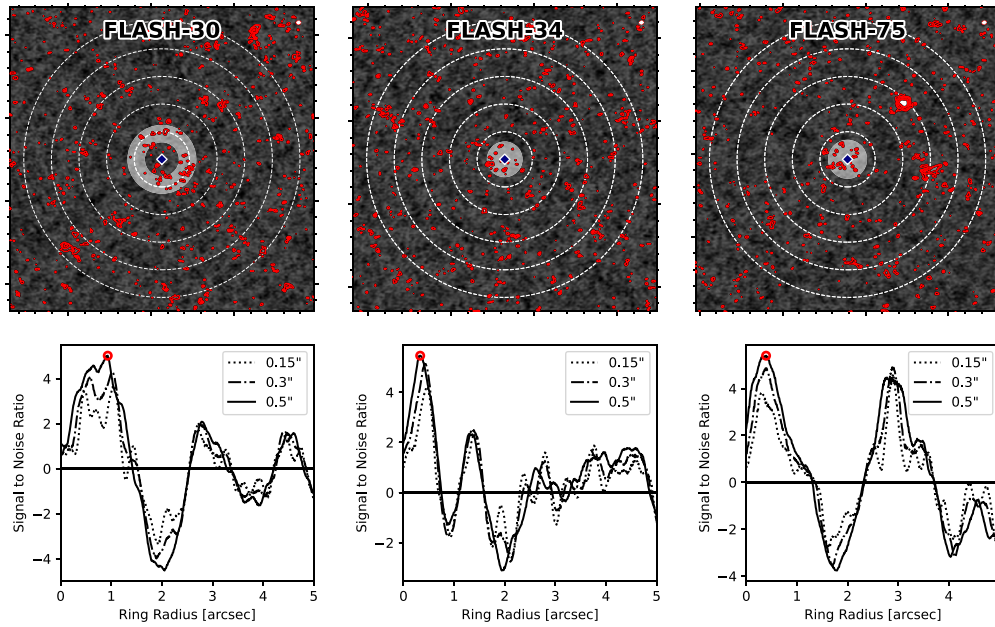
Figure 6. Top panels show a 11 by 11 arcsec view of the high-resolution (0.15 arcsec) ALMA continuum, with red contours at 2σ, 3σ, 5σ, 8σ, 10σ, and 20σ, with the dashed contours indicating negative continuum at the same levels. The blue diamond shows the VIKING position, with centred circles at 1, 2, 3, 4, and 5 arcsec in radius. The filled contour indicates the most significant emitting annulus. The bottom panels show the annulus-integrated signal-to-noise of the sources as a function of the ring radius for three different annulus widths. These three sources are the only sources where lensing was not already identified through direct observations, and the signal-to-noise in one of the three annuli exceeds 5σ.
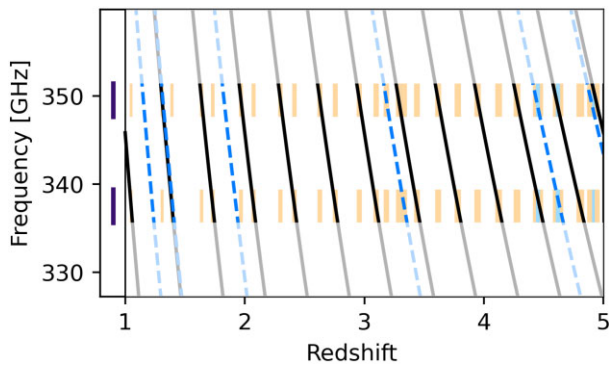
Figure 7. The ALMA observations have the ability to detect spectroscopic features. As galaxies red-shift, different lines come into view. The black lines indicate the CO lines, starting at CO(3-2) on the left-hand side. The blue lines indicate alternative lines we can expect to detect, such as [C I], H_2O, and [N II]. The graph was made using the redshift-search-graph tool by Bakx & Dannerbauer (2022), which highlights redshift regions where single CO lines are targeted are shown in orange fill. No redshift regions would expect more than a single CO line detection, although combinations of [C I], H_2O, and CO lines are still possible.

individual distances towards our telescope, and the mass distribution of the source. For a Single Isothermal Sphere (SIS) mass profile, the resulting angular separation between the centre-of-mass of the foreground source and the dust emission, θ_E, can be simplified to the equation

$$\theta_E = 4\pi \left(\frac{\sigma_v}{c}\right)^2 \frac{D_{LS}}{D_S}. \tag{7}$$

In this equation, the velocity dispersion σ_v is taken to be $\sqrt{GM/2r_h}$, with the halo definition ratio (r_h) take as the $r_{200} = 3M/(4\pi\,200*\rho_{crit}(z_l))$, where $\rho_{crit}(z_l)$ is the critical density of the
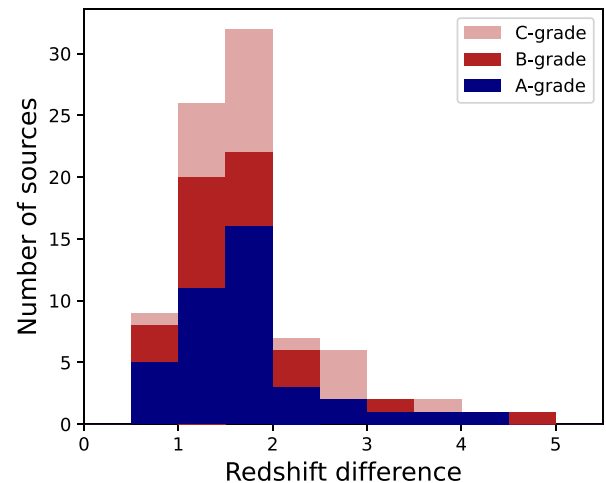

Figure 8. The distributions of the redshift difference between sources with different lensing classifications. The redshift difference distributions do not appear different between the A-, B-, and C-grade sources, suggesting there is no large contribution of confusion between foreground and background sources.

Universe at redshift z_l (Bartelmann & Schneider 2001). M is the total lensing mass, D_{LS} is the angular distance between the sub-mm source and the lens, and D_S represents the angular distance of the sub-mm source.

The VIKING catalogue provides a stellar mass based on a fit to the optical and NIR fluxes (Wright et al. 2019). In the case of galaxy–galaxy lensing, these sources are assumed to be massive cuspy systems, typically red-and-dead elliptical galaxies with little dust obscuration. Although the gas fraction of these galaxies is likely
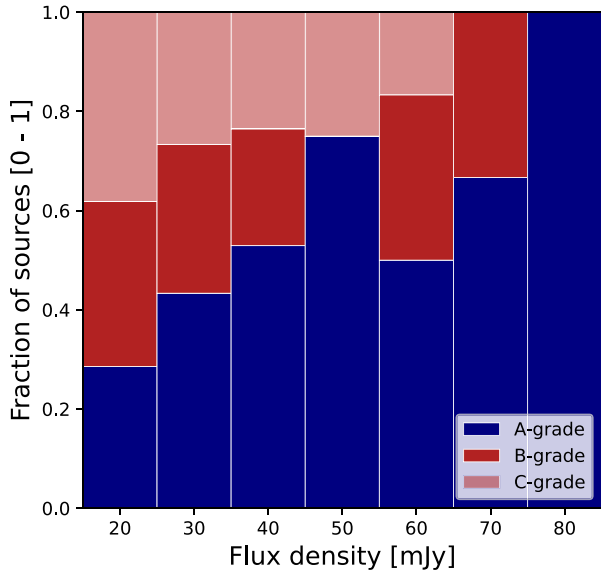
Figure 9. The fraction of sources in each classification is shown for each flux density interval at S_{500}. The different categories of sources are coloured in blue and red, with A-grade lens candidates in blue (bottom fill), B-grade candidates in dark red (middle fill), and C-grade candidates in light red (top fill, except for the top two flux bins). The number of confirmed lens candidates (A-grade) is highest for the brightest sources, although robust lensed sources are seen at all flux densities.
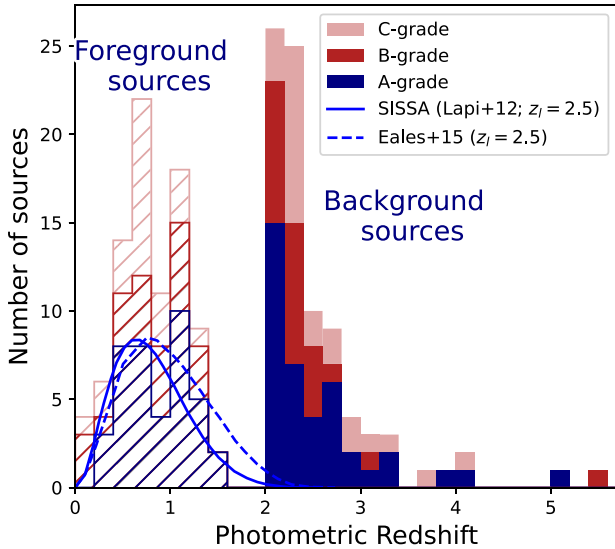

Figure 10. The foreground (*hatched histograms*) and background (*filled histograms*) redshift distribution of sources in A- (blue, bottom fill), B- (dark red, middle fill), and C-grade (light red, top fill). The foreground redshift distribution appears similar to the ones predicted from cosmological models (Lapi et al. 2012; Eales 2015, assuming $z_s = 2.5$). This suggests there is no obvious redshift bias in the foreground lensing distribution.

low – and the baryonic mass is thus locked up in the stars – the lensing mass of galaxies is dominated by the dark matter content of these sources. Cosmological models predict roughly a stellar-to-halo mass ratio of ~ 10–1000, depending on the halo mass (Girelli et al. 2020).

The ALMA observations provide a high-resolution view at the lensing geometry, and thus an estimate for θ_E. In Fig. 12, we compare the observed separation against the one predicted from the equation (7). The observed separation are taken from the weighted average of
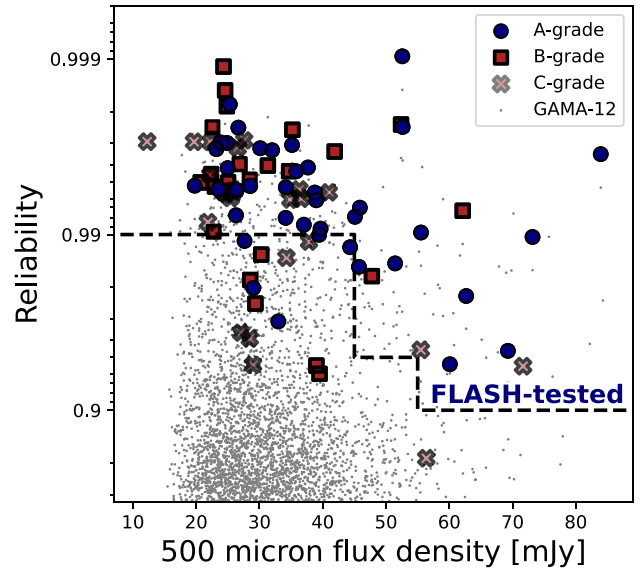
Figure 11. The distribution of sources as a function of their flux density and reliability for different source grades. There does not appear to be a clear correlation between the reliability and the nature of the source at these high reliabilities, likely because these sources pre-select towards *Herschel* positions scattered close to VIKING sources, which could pose a fundamental limit to the highest fidelity lens selection based on positions. Meanwhile, the method can accurately select lenses, even at lower reliabilities, enabling large lensing samples in the future. We show the underlying population of GAMA-12 sources with a similar selection function as the FLASH survey, as well as a line indicating the region where the FLASH observations are representative of the underlying population.
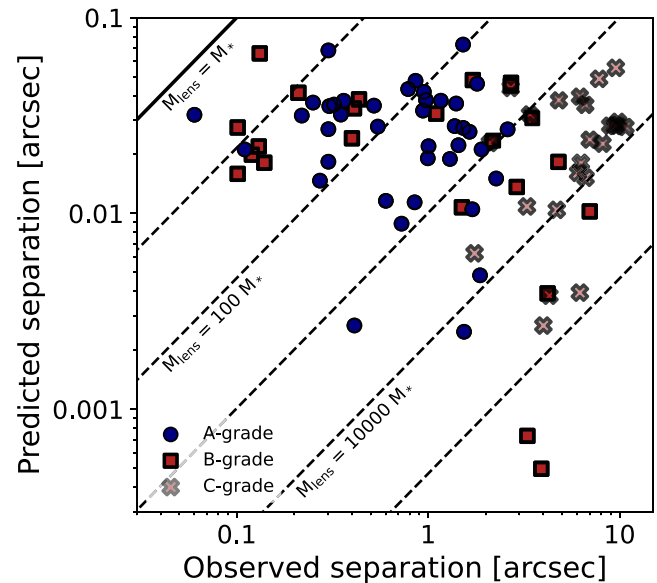

Figure 12. The expected separation based on the stellar mass estimates of the VIKING sources compared for the different source types. The lensing nature of the foreground sources depends on the total mass, including the enclosed dark-matter halo. The A-grade sources are located at lower lensing-to-stellar mass ratios. B-grade sources are split in two groups, with one group at low separation, while the other group suggests higher lensing-to-stellar mass ratios. C-grade sources are found at the highest separations, although they could still be lensed through galaxy–cluster lensing at larger separations.
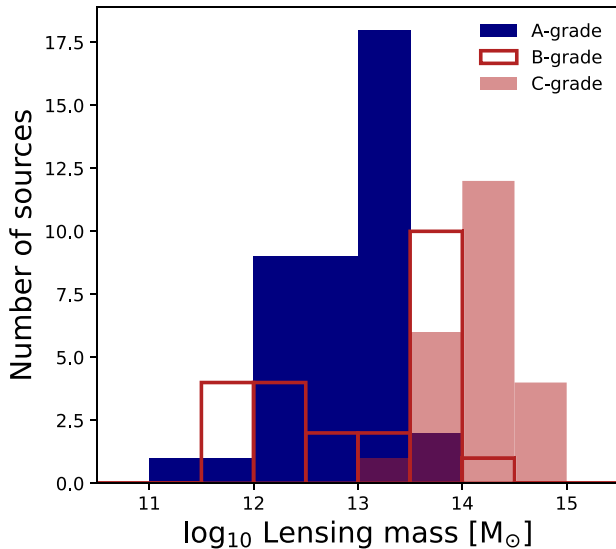
Figure 13. A histogram of the logarithm of the lensing mass expected from the observed angular separation between the foreground and background source, and the stellar mass derived from the VIKING photometry (Wright et al. 2019). It shows that the average mass of an A-grade lens candidates is $\log_{10} M/M_\odot = 12.9 \pm 0.5$. The B-grade candidates are more broadly distributed, and C-grade candidates lie at larger lensing masses if their ALMA emission is lensed by foreground VIKING galaxies, necessitating galaxy–cluster lensing events.

the positions of B- and C-grade lens candidates. For A-grade lens candidates, we select the weighted average of the angular separation of the sources that are the lensed counterpart (see Table 3). There is a clear distribution of sources based on their observed separation, although we note that this is part of the lensing grade identification. The A-grade sources are distributed below 2 arcsec. The B-grade sources are roughly distributed in two clumps, one group lies below 0.3 arcsec separation, where it is not possible to clearly differentiate between the foreground and background source, and the other group lies at separations above 1 arcsec. The C-grade sources are seen above 2 arcsec. A-grade sources are scattered around and below the predicted separation (i.e. $M_\mathrm{lens} = 100M_*$; see for example Crespo et al. 2022 and Fernandez et al. 2022), with masses between 10 and 1000 times the solar mass of the foreground system. Sources with B- and C-grades at higher separations could be more massive ($M_\mathrm{lens} > 1000M_*$) lensing events that are difficult to confirm with our current data. It is important to note that, although the Einstein radius used in equation (7) is correct for an SIS, the observed angular separation from the VIKING source to the ALMA-observed emission is an upper limit for θ_E. This measure also includes an additional factor that accounts for the source plane impact parameter, which can reduce the necessary mass to produce an observed offset. As a result, the most conservative approach would be to take the extreme offsets as upper limits.

We further compare the relative mass estimates of the sources in Fig. 13, where we show the mass of the foreground system, based on the angular offset between the ALMA and VIKING source, and the stellar mass of the foreground source. The average mass for the A-grade lens candidates is $\log_{10} M/M_\odot = 12.9 \pm 0.5$, and lies approximately one order of magnitude below the C-grade sources. The uncertainty in the lensing mass is well below one order of magnitude, and results from a combination in uncertainty in redshift and stellar mass. The effect of redshift has been studied in Serjeant

(2012), who reports a relatively minor variation (<50 per cent) for a large deflector redshift variation between $z_d = 0.3$ and $z_d = 1.5$ for a lensed source at redshift $z_l = 2.5$. The uncertainty in the stellar masses is also relatively low; however, we should consider that these observations target a very specific galaxy population, which could introduce a systemic uncertainty in stellar masses. That said, the stellar masses are unlikely to exceed much beyond 10^{11} M$_\odot$, and due to the square-root coefficient in equation (7), the resulting uncertainty will also be below 50 per cent (<0.2 dex, Wright et al. 2019). We estimate the halo-to-stellar mass ratio of our A-grade lens candidates, which is around $10^{2.2 \pm 0.1}$ M$_\odot$, with a source-to-source variation on the order of 0.9 dex. These values are in line with previous works from Amvrosiadis et al. 2018, Crespo et al. 2022, and Fernandez et al. 2022. Halo-to-stellar mass ratios in excess of 100 are high for dark matter haloes, although the profile taken in equation (7) assumes all the mass to be located solely at θ_E. Similarly, galaxies could be lensed by a group ($N < 5$) of sources, which would not be included in the stellar mass estimate from Wright et al. (2019). The mass ratio is around 0.5 dex, higher than those predicted in models from Girelli et al. (2020) for halo masses around $10^{12.9}$ M$_\odot$ around $z = 0$–1.

In part, this could be because of weak lensing affecting the sample (see further discussion of this in Section 4.4). Our lens identification method skews towards high-magnification, galaxy–galaxy lenses with cuspy profiles; however the VIKING images appear to indicate several fields with multiple galaxies, producing galaxy–cluster lensing missed in this analysis. Empirically, Dunne et al. (2020) found that weak lensing boosted the selection of even nearby ($z = 0.35$) galaxies. As a result of using direct ALMA observations to identify lensing, we are likely missing weak lensing events. As a consequence, higher mass haloes are likely contributing to the B- and C-grade sources, as shown in Fig. 13, although we note that it is necessary to account for the additional effect of the impact parameter of the sources, which is not perfectly represented by using the observed angular separation as θ_E in equation (7), as discussed above.

4.4 Total number of lenses in the *Herschel* catalogue

This is not the first search for gravitational lenses among the *Herschel* sample; however, it is one of the first study to comprehensively test the method across the *Herschel* fluxes using high-resolution sub-mm observations. In Fig. 14, we compare the source counts of sub-mm galaxies at 500 µm for both purely lensed candidate samples and non-differentiated samples. We compare these against the source counts of the lensed sources found by the FLASH method across the 53.56 square degree GAMA-12 field. We use the success ratio of the FLASH observations across the regime where the observations are representative for the underlying GAMA-12 field (see Fig. 11), and calculate the number of lensed sources that the current FLASH configuration will be able to identify. At the faintest flux end, we include an adjustment to show the effect of the 250 µm selection in light red: In the original *Herschel* catalogues, sources are extracted by their S_{250} flux density, removing some of the highest redshift galaxies. We adjust this by comparing the fraction of sources with low redshift ($z < 2$) to high redshift ($z > 2$) for the lowest two flux bins when compared with the highest flux bins.

The lensed candidates from the SHALOS method from González-Nuevo et al. (2019) and the VIKING-based selection from Ward et al. (2022) are compared against the non-differentiated selections from *Planck* (Trombetti et al. 2021), the brightest *Herschel* galaxies from Negrello et al. (2017), and the recent discovery of a lens among the STUDIES sample (Pearson et al. 2023). Surveys from SCUBA-
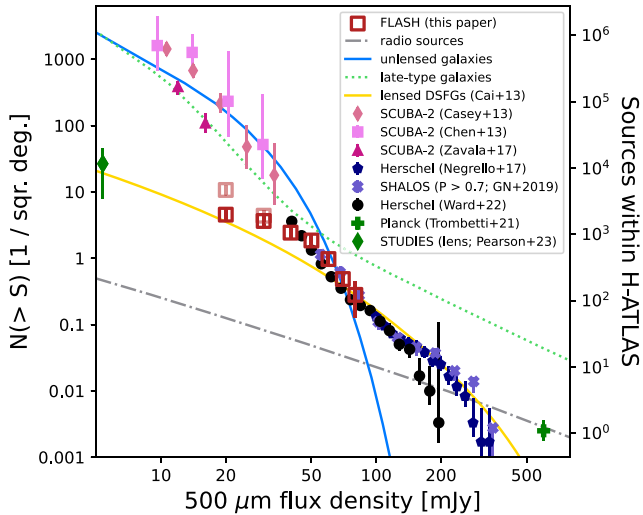
Figure 14. Cumulative number counts at 500 μm for the lensed sources in the FLASH sample and other samples – both pre-selected to contain lenses and without lens-pre-selections. Red squares indicate the number counts for all *Herschel* sources based on the FLASH selection and light-red squares show the source counts including an additional correction for the redshift-incompleteness towards lower flux densities. The counts of late-type, normal, and starburst galaxies and of unlensed DSFGs, interpreted as protospheroidal galaxies in the process of forming the bulk of their stars, are from the Cai et al. (2013) model, as well as the solid yellow line indicating the source counts for lensed sources with a magnification cut-off at $\mu_{max} = 15$ extending out to high fluxes. As seen in previous studies, these counts exceed the predicted number counts for lensed sources in the 10–60 mJy regime, as these models only account for strong galaxy–galaxy lensing, and do not account for galaxy–cluster lensing or weak lensing events potentially identified by the FLASH method.

2 at 450 μm from Casey et al. (2013), Chen et al. (2013), and Zavala et al. (2017) explore the lower flux-density regime. Note that all lensed candidate samples are based on unresolved predictions. We compare the sources against the different known 500 μm-bright emitters, namely late-type local galaxies at the brightest end, radio sources, lensed galaxies from the galaxy evolution model of Cai et al. (2013, assuming a maximum lensing magnification of $\mu_{max} = 15$), and finally unlensed DSFGs.

The predicted number of lenses found with the method described in Bakx, Eales & Amvrosiadis (2020a) is in agreement with the predicted values from Ward et al. (2022) and with those found in the SDSS-based estimates by González-Nuevo et al. (2019), even though the SDSS have been shown to be incomplete for the highest redshift lenses (Bakx, Eales & Amvrosiadis 2020a). Similar to previous statistical studies, we now robustly confirm the elevated number of lensed sources starting at ∼60 mJy when compared with strong lensing models. These models only account for galaxy–galaxy lensing, which misses galaxy–cluster lenses that have already been shown to dominate at lower flux densities through unresolved statistical studies (González-Nuevo et al. 2012, 2014). Although these galaxy–cluster lenses are an important contributor to the total number of lensed sources, identifying these systems is difficult given the requirement for deeper observations at larger FoVs. As noted in Ward et al. (2022), the likelihood estimator is not well-suited for the large separations of galaxy–cluster lenses (∼20 arcsec), and even misses the majority of galaxy–galaxy sources with separations above 8 arcsec. Our research is unable to quantify the galaxy–cluster lensing beyond a tentative visual tally of 12 fields with excess VIKING

sources, particularly in B- and C-grade fields. Meanwhile, these sources would still not be able to account for the 0.7 dex excess relative to the predicted models. The most likely explanation is the contribution of weak lensing, since the galaxy evolution models have a minimum classification of strong lensing at $\mu > 2$, and some of our sources might be only weakly magnified. This is corroborated by a visual inspection of our sources finds some sources with lensing identification (i.e. grade A) without multiple imaging or a counter-image resolved in the ALMA imaging. Although this does not exclude strong lensing. The contribution of weak lensing from our subsample of 18 sources without multiple imaging (FLASH-3, -12, -14, -20, -28, -30, -34, -37, -46, -47, -52, -54, -60, -61, -65, -68, -69, and -71) would nearly double (18/40 = 45 per cent) the number of strongly lensed sources when compared with the $\mu > 2$ strong lensing criterion adopted by Cai et al. (2013). This is on the same order as the excess of lenses seen between the lenses found by FLASH against those predicted in the galaxy evolution model of Cai et al. (2013).

For sub-mm galaxies with a redshift around 2.5, the likelihood of the flux at 250 micron being close to the detection limits increases as the flux density at 500 micron becomes fainter. This is a consequence of the detection strategy employed to construct the official H-ATLAS catalogues, as previously mentioned. Consequently, some of these sources are detected primarily due to lensing amplification, even with relatively small amplification factors ranging from 5 per cent to 20 per cent. This phenomenon, known as magnification bias, has received considerable attention in recent years and has been the subject of detailed measurement and analysis (Bonavera, Cueli & Gonzalez-Nuevo 2022 provides a concise overview of the topic).

Notably, the halo masses of the lenses, derived from the analysis of the cross-correlation function, exhibit a strong agreement with those estimated directly from individual lensing events in this study, yielding an approximate range of $10^{12-12.5}$ (González-Nuevo 2017, 2021; Bonavera et al. 2019, 2021; Cueli et al. 2021, 2022). Furthermore, these studies have concluded that the majority of magnification bias arises not from isolated galaxies, but from small groups of galaxies featuring one or two dominant members and a few satellites (see also Crespo et al. 2022; Fernandez et al. 2022). Therefore, it is likely that some of the lensing events observed in the current sample are also caused by small groups of galaxies. While there are indications in the images, verifying these observational findings would require data beyond the scope of this study.

Finally, similar to the discoveries made by Dunne et al. (2020), a few of the lensing events examined in this work can be considered as direct observations of magnification bias, which is typically studied only at a statistical level. In the study by Dunne et al. (2020), weak lensing modestly biased their fluxes even in the low-redshift Universe, although further investigations of the cluster-lensing population is necessary to see whether the excess is indeed due to galaxy–cluster lenses or whether an excess of lensed sources exist – an important point indeed, since this would require additional masses to exist beyond the ones predicted in our current cosmological paradigm (e.g. Eales 2015).

Accounting for the efficiency and the strict selection criteria of our sample, a total of 3000 lenses are expected to be observable across the 660 square degree H-ATLAS survey. This assumes the existence of complete VIKING-level observations, which are non-existent in the Northern field to date. This is large relative to the SHALOS method described in González-Nuevo et al. (2019) that provides a sample – adjusted for the total 660 square degrees of H-ATLAS –

of ~870 robust lensed candidates. The Southern-field study of Ward et al. (2022) has already demonstrated efficient selection of lensed sources down to ~30 mJy at 500 μm, and they report the ability to find 13 730 lensed sources across the entire H-ATLAS fields, which suggests it is worthwhile to test the FLASH method more comprehensively down to lower reliabilities as shown in Fig. 11.

At the lowest 500 μm flux densities, the H-ATLAS survey thins out significantly due to the prior selection at 250 μm in the catalogues. Lensed sources, located at redshifts above 2.5, would have lower fluxes at 250 μm. Our estimate based on the photometric redshift estimates of the entire *Herschel* catalogues, the expected number of sources across the full *Herschel* catalogues could be expanded to 7000 sources (a 2.35 times increase if we remove our current $\sigma_{250} \approx 7$ mJy criterion). These sources would be worthwhile to include in future lensing models, since (i) these sources have a larger cosmic volume for foreground lenses to magnify the background population and (ii) higher redshift galaxies are rarer in 500 μm-selected samples. Their steeper luminosity function (Gruppioni et al. 2013) ensures that more of the apparently bright high-redshift population is instead fainter gravitationally lensed sources. Future works could further improve lens selection by investigating samples that explicitly overcome this 250 μm selection, either through re-extraction (Ivison et al. 2016; Oteo et al. 2017) or through 500−250 μm difference maps (Asboth et al. 2016; Duivenvoorden et al. 2018). That said, the current methods are already powerful enough to enable large sub-mm selected lens samples (e.g. Eales 2015), and an ALMA survey of such large lens samples could become an important cosmological tool in the near future.

5 CONCLUSIONS

The *Herschel Space Observatory* detected near 1 million sources across 1000 square degrees from low to high redshift. In this study, we observationally test the validity of the selection method through resolved observations with ALMA, by targeting a sample of 86 likely lensed sources identified by close, bright VIKING counterparts. We find:

(i) The ALMA observations are able to confirm 40 (47 per cent) of these sources to be strong lenses (A-grade lens candidates). For an additional 23 (27 per cent) sources, there are tentative indications of lensing; however, our ALMA observations are not able to conclusively indicate lensing (B-grade lens candidates). For the final 23 (27 per cent), it remains unclear whether these sources are lensed (C-grade lens candidates).

(ii) The number of robust lensed sources is below what is expected from false-positive estimations, although we note that our current false-positive estimations might not be a reliable estimator, and future tests can focus on a more comprehensive study of $R > 0.9$ sources to verify the FLASH method and increase the number of lensed *Herschel* sources we can identify.

(iii) Although we do not find direct indication for sources where the VIKING galaxy and *Herschel* source are the same object, NIR spectroscopic confirmation of the foreground objects and sub-mm spectroscopic confirmation of the background sources is important to exclude such sources, particularly for the B-grade lens candidates below 1 arcsec separation.

(iv) Most of the lensing features would require a total lensing mass between 10 and 1000 times that of the stellar emission reported for these VIKING sources, with typical lensing masses of $\log_{10} M/M_\odot = 12.9 \pm 0.5$, in line with previous observations (Amvrosiadis et al. 2018) and above what is predicted from models (Girelli et al. 2020).

The ALMA identification method likely misses several sources at larger angular separations, potentially due to weak gravitational lensing.

(v) Our method will be able to find ~3000 lensed sources over the entire H-ATLAS field, in excess of what is expected from the galaxy–galaxy strong lensing predicted by the galaxy evolution models of Cai et al. (2013).

DATA AVAILABILITY

The reduced, calibrated, and science-ready ALMA data are available from the ALMA Science Archive at https://almascience.eso.org/asax/.

REFERENCES

ALMA Partnership et al., 2015, ApJ, 808, L4
Amvrosiadis A. et al., 2018, MNRAS, 475, 4939
Andrews B. H., Thompson T. A., 2011, ApJ, 727, 97
Asboth V. et al., 2016, MNRAS, 462, 1989
Bakx T. J. L. C., Dannerbauer H., 2022, MNRAS, 515, 678
Bakx T. J. L. C. et al., 2018, MNRAS, 473, 1751
Bakx T. J. L. C., Eales S., Amvrosiadis A., 2020a, MNRAS, 493, 4276
Bakx T. J. L. C. et al., 2020b, MNRAS, 494, 10
Bartelmann M., Schneider P., 2001, Phys. Rep., 340, 291
Baugh C. M., Lacey C. G., Frenk C. S., Granato G. L., Silva L., Bressan A., Benson A. J., Cole S., 2005, MNRAS, 356, 1191
Bendo G. J. et al., 2023, MNRAS, 522, 2995
Bonavera L. et al., 2019, J. Cosmol. Astropart. Phys., 2019, 021
Bonavera L., Cueli M. M., González-Nuevo J., Ronconi T., Migliaccio M., Lapi A., Casas J. M., Crespo D., 2021, A&A, 656, A99
Bonavera L., Cueli M. M., Gonzalez-Nuevo J., 2022, in Ruffini R., Vereshchagin G., eds, Proceedings of the MG16 Meeting on General Relativity. World Scientific Press, Singapore
Bourne N. et al., 2016, MNRAS, 462, 1714
Bussmann R. S. et al., 2013, ApJ, 779, 25
Bussmann R. S. et al., 2015, ApJ, 812, 43
Cai Z.-Y. et al., 2013, ApJ, 768, 21
Casey C. M. et al., 2013, MNRAS, 436, 1919
Chen C.-C., Cowie L. L., Barger A. J., Casey C. M., Lee N., Sanders D. B., Wang W.-H., Williams J. P., 2013, ApJ, 776, 131
Crespo D., González-Nuevo J., Bonavera L., Cueli M. M., Casas J. M., Goitia E., 2022, A&A, 667, A146

Cueli M. M., Bonavera L., González-Nuevo J., Lapi A., 2021, A&A, 645, A126

Cueli M. M., Bonavera L., González-Nuevo J., Crespo D., Casas J. M., Lapi A., 2022, A&A, 662, A44

Duivenvoorden S. et al., 2018, MNRAS, 477, 1099

Dunne L., Bonavera L., Gonzalez-Nuevo J., Maddox S. J., Vlahakis C., 2020, MNRAS, 498, 4635

Dye S. et al., 2015, MNRAS, 452, 2258

Dye S. et al., 2018, MNRAS, 476, 4383

Dyson F. W., Eddington A. S., Davidson C., 1920, Phil. Trans. R. Soc. A, 220, 291

Eales S. A., 2015, MNRAS, 446, 3224

Eales S. et al., 2010, PASP, 122, 499

Fernandez L., Cueli M. M., González-Nuevo J., Bonavera L., Crespo D., Casas J. M., Lapi A., 2022, A&A, 658, A19

Fleuren S. et al., 2012, MNRAS, 423, 2407

Furlanetto C. et al., 2018, MNRAS, 476, 961

Garratt T. K. et al., 2023, MNRAS

Girelli G., Pozzetti L., Bolzonella M., Giocoli C., Marulli F., Baldi M., 2020, A&A, 634, A135

González-Nuevo J. et al., 2012, ApJ, 749, 65

González-Nuevo J. et al., 2014, MNRAS, 442, 2680

González-Nuevo J. et al., 2017, J. Cosmol. Astropart. Phys., 2017, 024

González-Nuevo J. et al., 2019, A&A, 627, A31

González-Nuevo J., Cueli M. M., Bonavera L., Lapi A., Migliaccio M., Argüeso F., Toffolatti L., 2021, A&A, 646, A152

Grillo C., Lombardi M., Bertin G., 2008, A&A, 477, 397

Gruppioni C. et al., 2013, MNRAS, 432, 23

Harrington K. C. et al., 2021, ApJ, 908, 95

Hughes D. H. et al., 1998, Nature, 394, 241

Ivison R. J., Smail I., Le Borgne J. F., Blain A. W., Kneib J. P., Bezecourt J., Kerr T. H., Davies J. K., 1998, MNRAS, 298, 583

Ivison R. J. et al., 2016, ApJ, 832, 78

Kamieneski P. S. et al., 2023, preprint (arXiv:2301.09746)

Kelly P. L. et al., 2018, Nature Astron., 2, 334

Kneib J.-P., Natarajan P., 2011, A&AR, 19, 47

Kochanek C. S., 1992, ApJ, 384, 1

Kochanek C. S., 1996, ApJ, 473, 595

Lagos C. d. P., da Cunha E., Robotham A. S. G., Obreschkow D., Valentino F., Fujimoto S., Magdis G. E., Tobar R., 2020, MNRAS, 499, 1948

Lapi A. et al., 2011, ApJ, 742, 24

Lapi A., Negrello M., González-Nuevo J., Cai Z. Y., De Zotti G., Danese L., 2012, ApJ, 755, 46

Maddox S. J. et al., 2018, ApJS, 236, 30

Narayanan D. et al., 2015, Nature, 525, 496

Negrello M. et al., 2010, Science, 330, 800

Negrello M. et al., 2014, MNRAS, 440, 1999

Negrello M. et al., 2017, MNRAS, 465, 3558

Oguri M. et al., 2012, AJ, 143, 120

Oliver S. J. et al., 2012, MNRAS, 424, 1614

Oteo I. et al., 2017, ApJ, 850, 170

Overzier R. A., 2016, A&AR, 24, 14

Pearson E. A. et al., 2013, MNRAS, 435, 2753

Pearson J. et al., 2023, preprint (arXiv:2309.00888)

Planck Collaboration VI, 2020, A&A, 641, A6

Rizzo F., Vegetti S., Powell D., Fraternali F., McKean J. P., Stacey H. R., White S. D. M., 2020, Nature, 584, 201

Roseboom I. G. et al., 2010, MNRAS, 409, 48

Rowan-Robinson M. et al., 2016, MNRAS, 461, 1100

Rybak M., McKean J. P., Vegetti S., Andreani P., White S. D. M., 2015, MNRAS, 451, L40

Scudder J. M., Oliver S., Hurley P. D., Griffin M., Sargent M. T., Scott D., Wang L., Wardlow J. L., 2016, MNRAS, 460, 1119

Serjeant S., 2012, MNRAS, 424, 2429

Shirley R. et al., 2021, MNRAS, 507, 129

Smail I., Ivison R. J., Blain A. W., 1997, ApJ, 490, L5

Spilker J. S., Bezanson R., Marrone D. P., Weiner B. J., Whitaker K. E., Williams C. C., 2016, ApJ, 832, 19

Sutherland W., Saunders W., 1992, MNRAS, 259, 413

Tamura Y., Oguri M., Iono D., Hatsukade B., Matsuda Y., Hayashi M., 2015, PASJ, 67, 72

Treu T., 2010, ARA&A, 48, 87

Trombetti T., Burigana C., Bonato M., Herranz D., De Zotti G., Negrello M., Galluzzi V., Massardi M., 2021, A&A, 653, A151

Valiante E. et al., 2016, MNRAS, 462, 3146

Vieira J. D. et al., 2013, Nature, 495, 344

Ward B. A. et al., 2022, MNRAS, 510, 2261

Welch B. et al., 2022, ApJ, 940, L1

Wright A. H. et al., 2019, A&A, 632, A34

Zavala J. A. et al., 2017, MNRAS, 464, 3369

SUPPORTING INFORMATION

Supplementary data are available at *MNRAS* online.

Table 1. FLASH catalogue.

Table 3. ALMA observations catalogue.

Please note: Oxford University Press is not responsible for the content or functionality of any supporting materials supplied by the authors. Any queries (other than missing material) should be directed to the corresponding author for the article.

APPENDIX A: COMPILATION OF STRONG LENSES

We present a graphical depiction of strong lenses detected across the spread in 500 μm flux density in Fig. A1, showing the capability of FLASH to detect strong lenses down to $S_{500} = 20$ mJy.
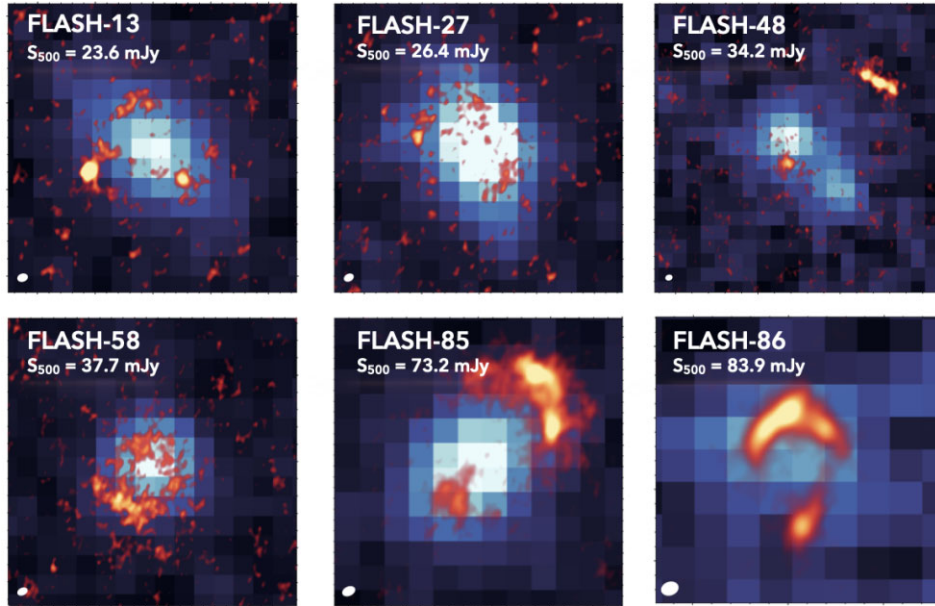
Figure A1. These six ALMA images (foreground red) indicate the ability of the FLASH method to select strong lenses by matching *Herschel* and VIKING images (background images) from low- to high-500 μm flux densities. The images are 5 arcsec across, except for FLASH-48 (7 arcsec), FLASH-85 (4 arcsec), and -86 (3 arcsec). The red foreground is drawn at 1σ and beyond for FLASH-13, -27, and -58, and it is drawn starting at 2σ for FLASH-48, -85, and -86 to best show the lensing behaviour and extent.

This paper has been typeset from a TEX/LATEX file prepared by the author.